UNIVERSITY OF OKLAHOMA

GRADUATE COLLEGE

Q ESTIMATE USING SPECTRAL DECOMPOSITION

A THESIS

SUBMITTED TO THE GRADUATE FACULTY

in partial fulfillment of the requirements for the

Degree of

MASTER OF SCIENCE

By

TOAN DAO
Norman, Oklahoma
2013

Q ESTIMATE USING SPECTRAL DECOMPOSITION

A THESIS APPROVED FOR THE
CONOCO PHILLIPS SCHOOL OF GEOLOGY AND GEOPHYSICS

BY

Dr. Kurt J. Marfurt, Chair

Dr. G. Randy Keller

Dr. Tim Kwiatkowski

ACKNOWLEDGEMENTS

This thesis would not have been possible without my adviser, Dr. Kurt J. Marfurt for giving me all the support, guidance and freedom to explore an ocean of knowledge without getting lost. From him I started to truly understand that learning is a lifetime process. When I complained about the new generations of students not adequately equipped with a solid foundation of the basic science, his response was: "You never will have all the technical skills you will need. Just watch me at 62 years old learning C++. Who would have thought I'd be learning my twelfth computer language?". Thank you for these words. I will carry them for many years ahead.

I would like to thank Dr. Tim Kwiatkowski and Dr. G. Randy Keller for their advice, encouragement and hours of code debugging. I would also like to send my special thanks Dr. Vikram Jayaram for helping me look into the problems with a different view and in the completion of the important writing process.

I owe my deepest gratitude to my family and all my friends.

Last but not least, I would like to thank the sponsors to the Attribute-Assisted Seismic Processing and Interpretation consortium for their financial support.

TABLE OF CONTENTS

LIST OF FIGURES

ABSTRACT

Attenuation is an important seismic property, especially in exploration seismology since it greatly influences seismic data quality. As the industry is shifting to explore ever thinner reservoirs, better understanding of attenuation can help to improve the data quality as well as characterize rock properties and reservoir heterogeneity.

Because of its capability to detect local changes, spectral decomposition using the Continuous Wavelet Transform can be used to quantify the quality factor Q (reciprocal of attenuation) over a seismic interval which for the case of this study will be between the top and the base of the Lower Barnett Shale. I introduce an improvement over the previously developed Inverse Continuous Wavelet Transform deconvolution. The maxima modulus lines (ridges) created by connecting the singularities obtained from spectral decomposition identify the strongest and the most continuous events. The maxima wavelet matrix formed by integrating along the maxima lines make up the basis functions to model the signal. A residual signal is obtained to which we can apply the same process to iteratively update the model. The modeled signal converges such that the strongest and most continuous information is updated first. This algorithm attempts to overcome two limitations of the Inverse Continuous Wavelet Transform deconvolution (Matos and Marfurt, 2011) that the amplitude of the reconstructed data is not preserved while only the largest events are represented and smaller amplitude events are removed.

Variable-window transforms decompose the data into frequency bands amenable to Q estimation using the spectral ratio technique. Before estimating Q, I pre-

condition the data using two passes of structured-oriented filter and spectral balancing. To furthermore enhance the signal-to-noise ratio, I use horizon-based Principal Component Analysis (PCA) to uncorrelate the spectral component data. The computed Q values are unrealistic due to the previous processing workflow and complexity of the geology.

Chapter 1

INTRODUCTION

1.1 Motivation

Seismic attenuation is one of the most fundamental mechanisms of elastic waves propagating through the earth. There are two coupled processes associated with attenuation: dissipation and dispersion. The dissipation process suppresses the seismic amplitude while the dispersion process distorts the phases. Attenuation acts as a time-variant low-pass filter with a monotonically increasing phase spectrum. The direct consequence of these processes on seismic data is that the seismic wavelet becomes more stretched and its amplitude becomes exponentially smaller with time and depth. These processes also contribute to the non-stationary behavior of the seismic wavelet and decreasing resolution with time and depth. As we explore for ever thinner and more subtle hydrocarbon reservoirs, improving the resolution by compensating for attenuation becomes more important. Furthermore, attenuation, if quantified, can be used as a seismic attribute to characterize rock properties, reservoir heterogeneity and the success of completion processes.

1.2 Previous work

Work on wave attenuation can be found in early literature in different fields, especially in physics and chemistry. Some of the most recent work to estimate Q includes Tonn (1991) who estimates attenuation using both time and frequency methods, and by Singleton et al. (2006) who decomposes the data using Gabor

wavelets. Wang (2008) attempts to correct for the attenuation effect rather than estimating it. His inverse filters correct for amplitude, phase or both at the same time. Van der Baan (2012) considers the inverse filter a bandwidth enhancement process that can be approximated by time-varying Wiener deconvolution.

Chapter 2 summarizes the theory of attenuation. Chapter 3 introduces spectral decomposition and data reconstruction using the maxima modulus line with a matching pursuit scheme. Chapter 4 shows how to precondition the the spectral components using complex Principal Component Analysis. These filtered data are then used to estimate Q using an iteratively reweighted least-squares spectral ratio method. Chapter 5 summarizes the results and discusses limitation of the method.

1.3 Hypothesis

The Fourier Transform measures the global periodicity of a signal resulting in coefficients for a suite of sines and cosines spanning the entire length of the seismic trace. The Continuous Wavelet Transform, on the other hand, uses the concept of a temporarily-windowed mother wavelet that is scaled, translated down the trace and then correlated with the signal to detect local changes with respect to time. Since attenuation changes the amplitude and phase of the signal with time, the Continuous Wavelet Transform can be used to estimate and compensate for attenuation effects.

Chapter 2

THEORY

2.1 Definitions and terminology

Attenuation is most commonly quantified by its reciprocal, Q, which stands for "quality factor". Seismic amplitude experiences both apparent attenuation and intrinsic attenuation. Apparent attenuation (Q_{app}^{-1}) includes geometric spreading, random scattering and layer-related phenomena such as reflection, transmission, multiple generation and mode conversion which are reversible and conserve energy (Liner, 2012). This type of attenuation is non-dispersive. In contrast, intrinsic attenuation (Q_{int}^{-1}) is the product of the conversion of elastic to heat energy due to internal friction (Aki and Richards, 1980). Unlike apparent attenuation, intrinsic attenuation is dispersive, is not as well understood as apparent attenuation, and is more difficult to quantify. The total attention (Q_{total}^{-1}) is the sum of the apparent attenuation and intrinsic attenuation:

$$Q_{total}^{-1} = Q_{app}^{-1} + Q_{int}^{-1}. \tag{2.1}$$

Attenuation is an anelastic property that can be used with other physical measurements to characterize rock properties (Johnston and Toksoz, 1981). The most common measure of attenuation is the reciprocal of the dimensionless quality factor Q. Q is defined in terms of the ratio of the maximum energy stored at maximum stress and strain, W, over the energy loss per cycle of a harmonic excitation, ΔW:

$$Q(\omega) = 2\pi \frac{W}{\Delta W}. \tag{2.2}$$

The attenuation coefficient α is defined in terms of Q using Kolsky's (1955) Q model:

$$\alpha = \frac{\omega}{2v}\frac{1}{Q(\omega)}, \tag{2.3}$$

where ω is the temporal frequency measured in radian/s and v is the phase velocity.

The amplitude A is proportional to $W^{1/2}$. Assuming $Q >> 1$, equation 2.2 can be rewritten in term of the ratio between the change in amplitude, ΔA over the amplitude, A:

$$\frac{1}{Q(\omega)} = \frac{1}{\pi}\frac{\Delta A}{A}. \tag{2.4}$$

The amplitude A decreases by $\frac{\pi}{Q}$ in one period $T = \frac{2\pi}{\omega}$. Therefore, the amplitude at time t, $A(t)$, can be written as

$$A(t) = A_0(1 - \frac{\pi}{Q})^n, \tag{2.5}$$

where A_0 is the amplitude at time $t = 0$ and $n = \frac{\omega t}{2\pi}$ is the number of periods. Taking the limit as $\omega t \to \infty$ gives:

$$A(t) = A_0 e^{-\frac{\omega t}{2Q}}. \tag{2.6}$$

Replacing $t = \frac{x}{v}$ to obtain the amplitude as a function of distance gives

$$A(x) = A_0 e^{-\frac{\omega x}{2vQ}}. \tag{2.7}$$

Equations 2.6 and 2.7 show that amplitude decreases exponentially with time and distance.

2.2 The effect of attenuation on a seismic pulse

Consider a delta function as a seismic pulse traveling with velocity v along the x axis in a viscoelastic medium characterized by the function $Q(z,\omega)$. To be able to derive the shape of the pulse at time t, I decompose the pulse into Fourier components

$$\mathcal{U}(z,\omega) = \int_{\mathbf{R}} \delta(t - \frac{z}{v}) e^{i\omega t} dt = e^{\frac{i\omega z}{v}}. \tag{2.8}$$

The pulse $u(z,t)$ at time t and location z is reconstructed by summing all the Fourier components after applying $Q(z,\omega)$ using equation 2.7:

$$u(z,t) = \frac{1}{2\pi} \int_{\mathbf{R}} e^{-\frac{\omega z}{2vQ(z,\omega)}} \mathcal{U}(z,\omega) e^{-i\omega t} d\omega. \tag{2.9}$$

Equation 2.9 does not have an analytic expression if $Q(z,\omega)$ is an arbitrary function. To simplify the calculation, I assume $Q(z,\omega)$ be a constant. Equation 2.9 now can be expressed as

$$u(z,t) = \frac{1}{\pi} \frac{\frac{z}{2vQ}}{(\frac{z}{2vQ})^2 + (\frac{z}{v} - t)^2}. \tag{2.10}$$

The pulse $u(z,t)$ at the same time t and location z is plotted in Figure 2.1 for different values of Q at different times. The shape of the pulse at time t is dictated by the value of Q. Lower values of Q (higher attenuation) will decrease the amplitude and broaden the wavelet. Higher values of Q (lower attenuation) will keep the amplitude and shape of the wavelet closer to the shape of the original pulse. An exponential curve can be fit to be tangential to all the peaks of the pulse, which is in agreement with the behavior of the amplitude

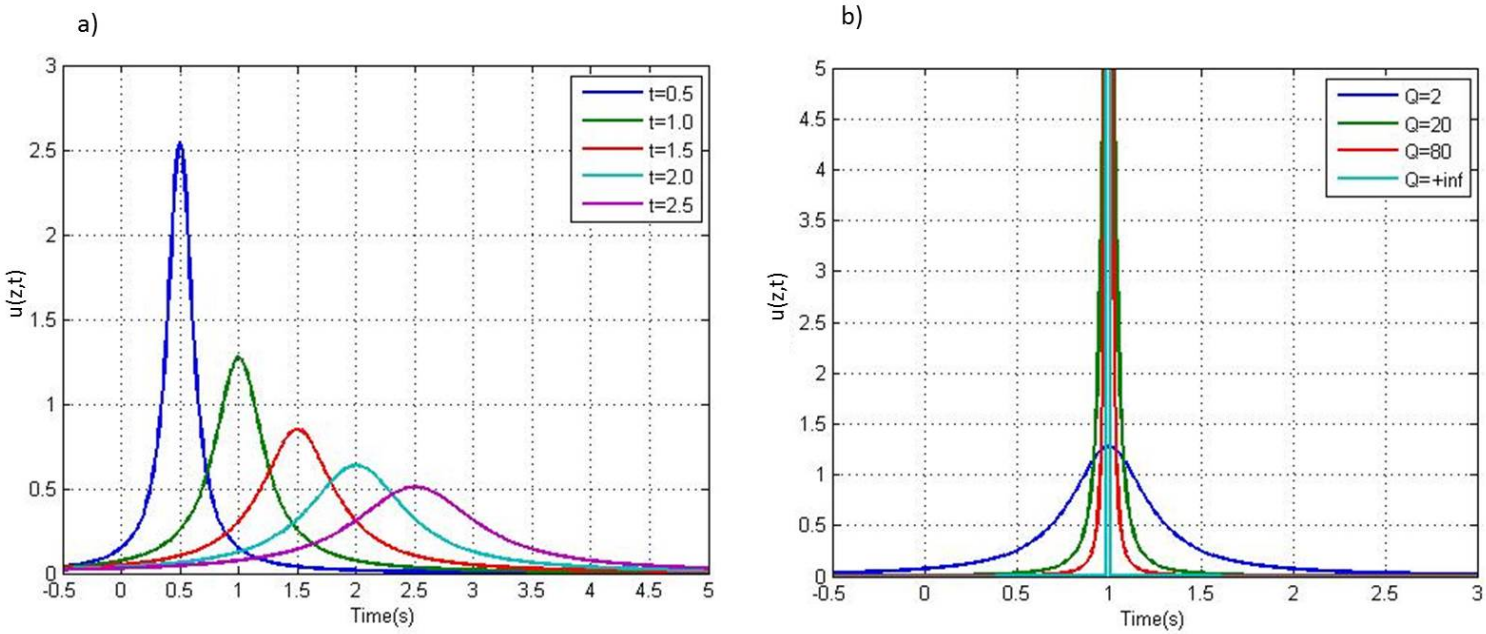

Figure 2.1. (a) Seismic pulse at times $t = 0.5, 1.0, 1.5, 2.0, 2.5$ s, constant $Q = 2$ and (b) seismic pulse at time $t = 1.0$s with different values of Q. Note that the attenuation operator does not modify the phase such that energy can arrive before $t = 0$ s.

in equation 2.7. Aki and Richards (1980) indicate that this constant-Q model is physically not possible because a pulse at any given time $t > 0$ and $Q \neq \infty$ can respond to the stress before it arrives, violating the causality principle. To address this problem, $Q(z, \omega)$ must be a function of ω. In general, higher frequencies will be attenuated faster and travel faster than lower frequencies.

2.3 The attenuation-dispersion relation

Let $u(z, t)$ be a vertically traveling plane wave at at position z and time t,

$$u(z,t) = \int S_0(\omega) e^{i(\omega t - kz)} d\omega \tag{2.11}$$

where k is the wavenumber and $S_0(\omega)$ is the source wavelet in the frequency domain. In an attenuating medium, k is a complex number

$$k = \frac{\omega}{v(\omega)} + i\alpha(\omega) = k_r(1 + \frac{i}{2Q(\omega)}), \tag{2.12}$$

where $\alpha(\omega)$ is the attenuation factor, $Q(\omega)$ is the quality factor and $v(\omega)$ is the phase velocity.

Futterman (1962) shows that attenuation and dispersion must be coupled such that $u(x, t)$ responds after the stress is applied at the source location. Using this result to guarantee the causality of the system, Aki and Richards (1980) derive the relationship connecting frequency ω, phase velocity $v(\omega)$ and attenuation factor $\alpha(\omega)$ to guarantee $u(z, t) = 0$ before the earliest possible arrival time $t = \frac{z}{v_\infty}$,

$$\frac{\omega}{v(\omega)} = \frac{\omega}{v_\infty} + \mathcal{H}[\alpha(\omega)], \tag{2.13}$$

where he defines $v_\infty = \lim_{\omega \to \infty} v(\omega)$ and the operator $\mathcal{H}$ denotes the Hilbert trans-

form. The phase of $u(z,t)$ depends on the the Hilbert transform of the attenuation factor $\alpha(\omega)$ which involves all the frequencies, giving rise to alternative Q models.

Q models for the phase velocity include Kolsky's (1955) constant-Q model, Strick's (1967) power law model, Kjartansson's (1979) model, M*ü*ller's (1983) model, Azimi et al.'s (1968) second and third model, the Cole-Cole (1941) model and the standard linear solid. Wang and Guo (2004) show that it is possible to modify the parameters of Kolsky's (1955) model to match the other models. Ursin and Toverud (2004) examined all these models and found all were equivalent in the 10-100 Hz seismic spectrum. All the Q models discussed require a reference phase velocity, v_0 and a reference frequency, ω_0. For instance, Futterman (1962) proposes a term γ_F

$$k = \frac{\omega}{v_0}[1 - \frac{1}{\pi Q}\ln(\frac{\omega}{\omega_0})] = \frac{\omega}{v_0}\gamma_F, \tag{2.14}$$

while Kjartansson (1979) models the wavenumber differently using γ_K

$$k = \frac{\omega}{v_0}(\frac{\omega}{\omega_0})^{-\frac{1}{\pi Q}} = \frac{\omega}{v_0}\gamma_K. \tag{2.15}$$

Substituting one of the above expressions for the wavenumber k into equation 2.11 gives

$$u(t,t_0) = \int S_0(\omega)\exp\Big[i\omega(t_0\gamma - t)\Big]\exp\Big(-\frac{\omega t_0\gamma}{2Q}\Big)d\omega, \tag{2.16}$$

where γ takes one of the functions γ_F or γ_K.

Equation 2.16 can be rewritten in term of the inverse Fourier transform of a

function:

$$u(t,t_0) = \mathcal{F}^{-1}\Big[S_0(\omega)\exp\Big(i\omega t_0\gamma\Big)\exp\Big(-\frac{\omega t_0\gamma}{2Q}\Big)\Big] \tag{2.17}$$

The first exponential term in equation 2.17 models the phase while the second exponential term models the amplitude of the wavelet. The reference phase velocity and frequency serve as a standard to compare the behavior at all other frequencies. For simplicity, let the source wavelet $s(t) = \delta(t)$, $S(\omega) = 1$, $Q = 30$, $v_\infty = 6250$ m/s, $v_0 = 5000$ m/s and $f_0 = 30$ Hz. Using equation 2.17 with Futterman's model, I obtain the temporal waveform and the spectral magnitude of the pulse at $z = 500$ m and plot them in Figure 2.2. The shape of the pulse spreads but dies out before time $t = \frac{z}{v_\infty} = 0.08$ s.

2.4 The effect of attenuation on seismic data

The earth acts as a low-pass filter in which the higher frequency components are suppressed more than the lower frequency components. This phenomenon causes a number of issues in seismic exploration as high frequencies are as important as low frequencies. First of all, attenuation lowers the seismic data quality if the high frequency components of the data fall below the noise level. Figure 2.3a shows a 2D line after acoustic inversion from seismic data without Q compensation. Figure 2.3b shows the same 2D line after acoustic inversion from data with Q compensation. In both figures, the white vertical lines outline the well log. The strata in Figure 2.3b match the well-log data better than those in Figure 2.3a. We immediately notice that Figure 2.3 contains higher frequencies and therefore shows more detail. Some of the structures are imaged better in this figure such as a fault at $x = 13$ km and $t = 4.0$ s. In Figure 2.3, this fault is more difficult to see since part of the high frequency data are missing.

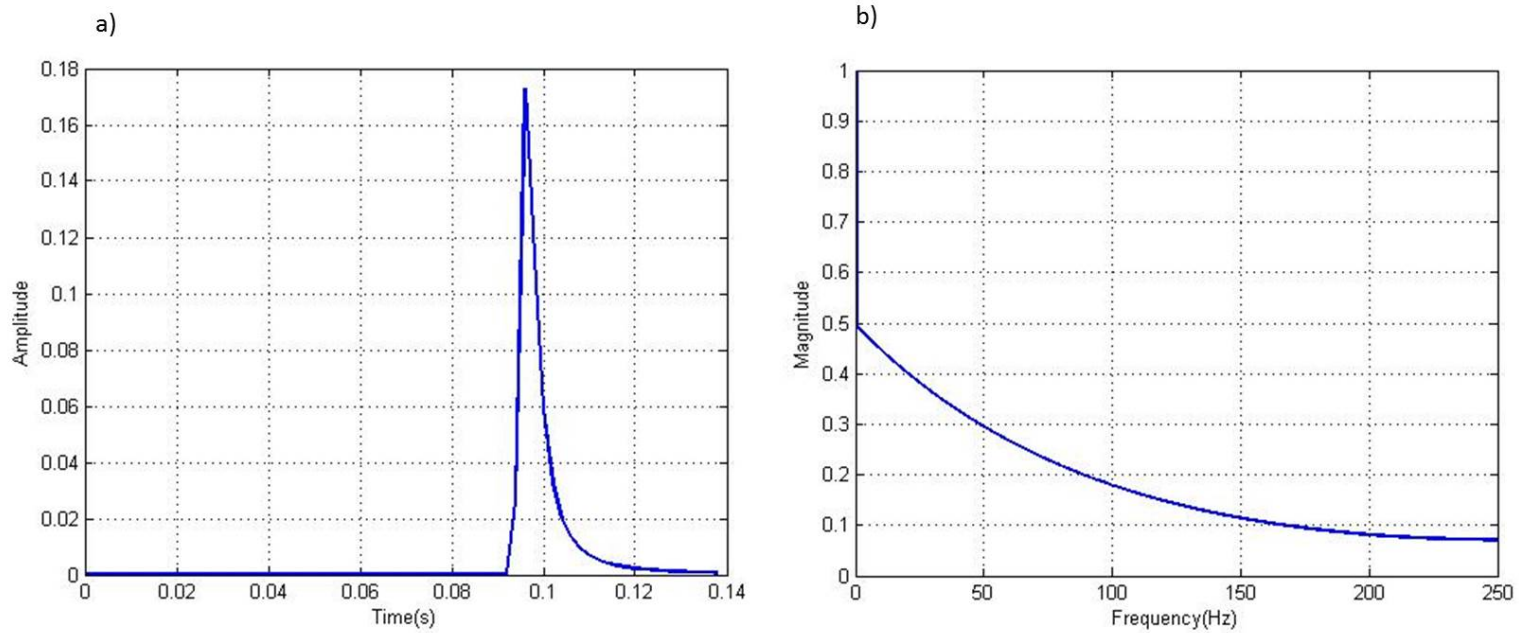

Figure 2.2. (a) The temporal waveform of the Dirac delta function from the origin after traveling a distance of $z = 500$ m with the reference velocity of $v_0 = 5000$ m/s in an attenuating medium with causality taken into account for $Q = 30$, $v_0 = 5000$ m/s and $f_0 = 30$ Hz and (b) its spectral maginitude. The area between the curve and 1 represents the amount of energy loss.

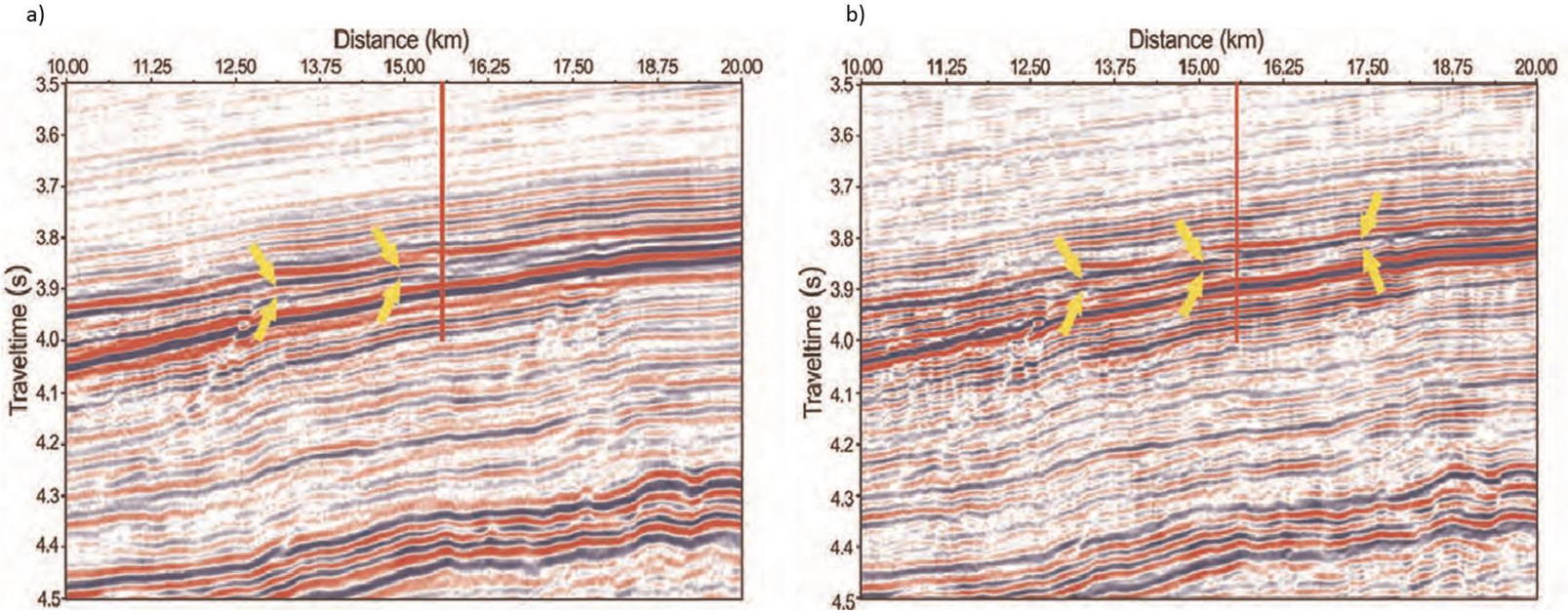

Figure 2.3. A 2D line through seismic amplitude data (a) without Q compensation and (b) with Q compensation. The yellow arrows indicate the reservoirs (after Wang, 2008).

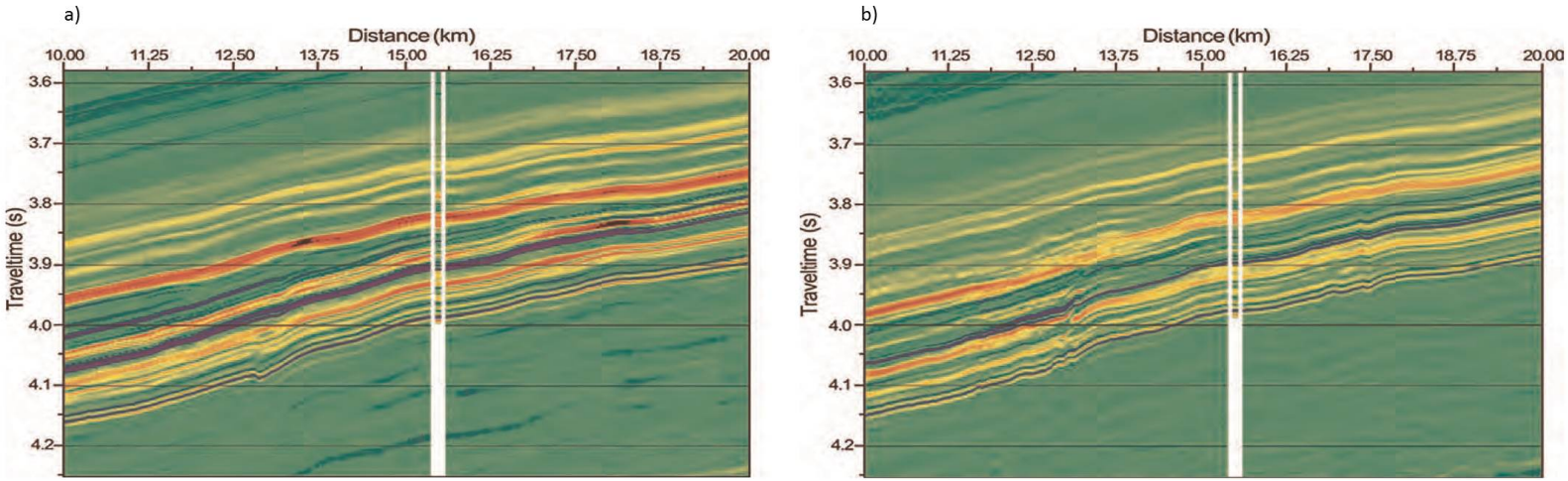

Figure 2.4. A 2D line through acoustic impedance computed from seismic data (a) without Q compensation and (b) with Q compensation (after Wang, 2008).

Figures 2.4 shows another example by Wang (2008) that demonstrates the effect of Q on seismic data. The reservoir indicated by the yellow arrows is better imaged with Q compensation. Part of the reservoir on the right of Figure 2.4a cannot be imaged or interpreted with the same confidence as that in Figure 2.4b. Through the Q compensation process, the frequency bandwidth is broadened and the waveform is squeezed and more symmetric.

2.5 Q estimation using the spectral ratio method

The spectral ratio method is a robust frequency-domain method to estimate Q. Given two points x_1, x_2 and their magnitude spectra $a_1(f)$, $a_2(f)$, Q is calculated between the two points by comparing the energy of the signal at all the available frequencies. For each frequency f, $a_2(f)$ can be expressed in terms of $a_1(f)$ and Q as:

$$a_2(f) = g(z_1, z_2)a_1(f)\exp\Big(\frac{-\pi f \Delta z}{Qv}\Big) \tag{2.18}$$

where $\Delta z = z_2 - z_1$ and $g(z_1, z_2)$ is a frequency-independent function incorporating the effects of spherical divergence, dependence of the pulse amplitude on impedance, source strength, recorder gain and angular dependence of the radiation pattern (Costag and Ernest, 1987).

Taking the natural logarithm of both side of equation 2.18 gives

$$\ln \frac{a_2(f)}{a_1(f)} = \ln g(z_1, z_2) - \frac{\pi f \Delta z}{Qv}. \tag{2.19}$$

or in terms of travel time:

$$\ln \frac{a_2(f)}{a_1(f)} = \ln g(t_1, t_2) - \frac{\pi f \Delta t}{Q}. \tag{2.20}$$

Cross-plotting $\ln \frac{a_2(f)}{a_1(f)}$ versus frequency f yields a linear relationship whose slope is $p = -\frac{\pi \Delta z}{Qv} = -\frac{\pi \Delta t}{Q}$, from which Q can be calculated.

2.6 Q estimation using the average frequency method

In an attenuating medium, the frequency spectrum of a wavelet is continuously changing where the amount of change is a function of Q. Treating f as a random variable with probability density function, $a^2(f)$, Hauge (1981) finds the average frequency,

$$\bar{f} = \int f a^2(f) df, \tag{2.21}$$

and variance

$$\sigma_f^2 = \int (f - \bar{f})^2 a^2(f) df \tag{2.22}$$

of the spectrum to be related by

$$\frac{d\bar{f}}{dz} = -\frac{2\pi}{Qv}\sigma_f^2, \tag{2.23}$$

or in terms of travel time:

$$\frac{d\bar{f}}{dt} = -\frac{2\pi}{Q}\sigma_f^2. \tag{2.24}$$

In practice, spectral ratio methods are more commonly used and are more robust than the average frequency method.

Chapter 3

SPECTRAL DECOMPOSITION

3.1 Spectral decomposition using the Continuous Wavelet Transform

The Continuous Wavelet Transform introduced by Morlet et al. (1982) is one of the more popular techniques used in spectral decomposition, breaking broadband seismic data into its time-frequency components. The mathematics of the Continuous Wavelet Transform is summarized in Appendix A.

Figures 3.1 show a representative seismic signal and its spectral magnitude and phase computed using the complex Morlet wavelets. A vertical slice of the spectrum describes the behavior of a particular frequency over time. Likewise a horizontal slice is the frequency profile at that specific time. The magnitude spectrum indicates that the frequencies range from 10-80 Hz and are localized at $t = 1.30$, 1.36, 1.40 and 1.45 seconds. Figure 3.2 shows a suite of frequency components of a vertical slice of the data. Note that the variation in each of the magnitude components can be observed. The vertical slice through the original data is shown in Figure 3.14a.

3.2 Singularities and the Maxima Wavelet Matrix

Mallat (2009) defined singularities in the complex time-frequency domain, $c(j, f)$, as the local maxima of the magnitude of the CWT coefficients along the time axis (Figure 3.1b). Mallat (2009) noted that singularities associated with the spectral peaks form ridges in the time-frequency domain, which when

convolved with the corresponding wavelet and summed represent the more important features of the original input seismic trace. Rather than use the corresponding wavelet at each frequency component to reconstruct the data, Matos and Marfurt (2011) convolved the maximum modulus lines (ridges) (MML) with a broader band wavelet, thereby extending the bandwidth of the data, resulting in what they called inverse continuous wavelet transform deconvolution (ICWTD). There are two limitations of both Mallat (2009) and Matos and Marfurt's (2011) algorithms. First, the amplitude of the reconstruction is not preserved, while second, only the largest events are represented, such that smaller amplitude but perhaps important events are removed.

The maxima wavelet matrix, $\mathbf{W}$, is formed by integrating along the sets of connected singularities (ridges) after placing the center of the wavelet $\psi_{f,\tau}(t)$ at each singularity. $\mathbf{W}$ forms the basis for the input signal $\mathbf{d}$ where the j^{th} column $\mathbf{w}_j$ is localized about the time of the j^{th} ridge. In general, the singularities fall between discrete samples. Although assigning the ridges for purposes of QC to the nearest sample such as shown in Figures 3.1d and e are adequate for display purposes, a more accurate estimate will improve the temporal resolution of the maxima wavelet matrix. I therefore fit a parabola between $c(t_{j-1}, f), c(t_j, f)$ and $c(t_{j+1}, f)$ about each peak to obtain the peak time at a fractional sample values prior to summation.

3.3 Spectral decomposition using the maxima modulus lines with a matching pursuit scheme

Figure 3.4 demonstrates the flowchart of the matching pursuit algorithm to decompose the data into the ridge components. I modify Mallat's (2009)'s

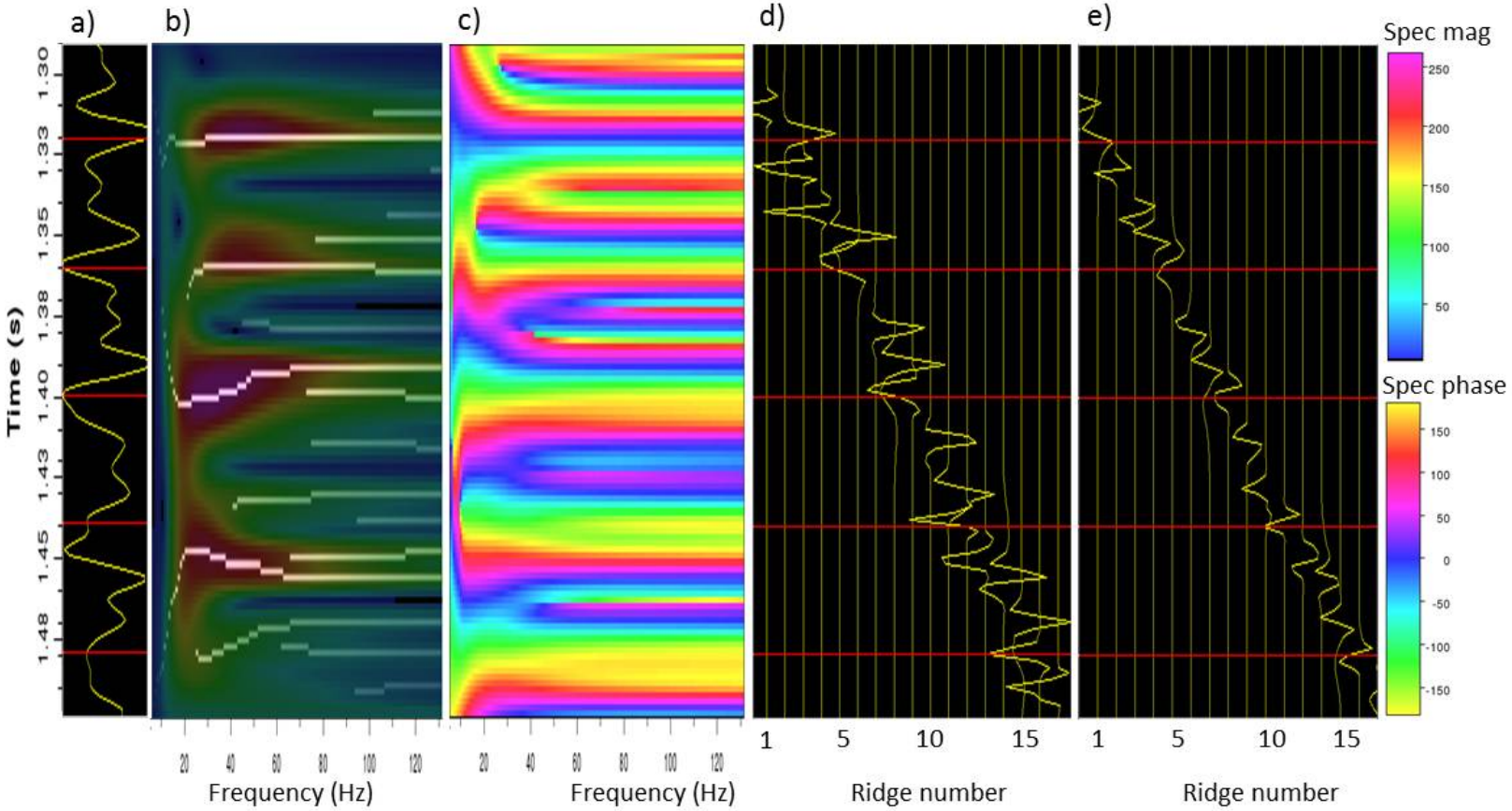

Figure 3.1. A (a) representative seismic data trace, *d(t)*, (b) its spectral magnitude components co-rendered with the maxima modulus lines (ridges), (c) its spectral phase components $c(t, f)$, (d) the real part of the J=17 composite wavelets generated by integrating over the ridges and (e) the imaginary part of the J=17 composite wavelets generated by integrating over the ridges.

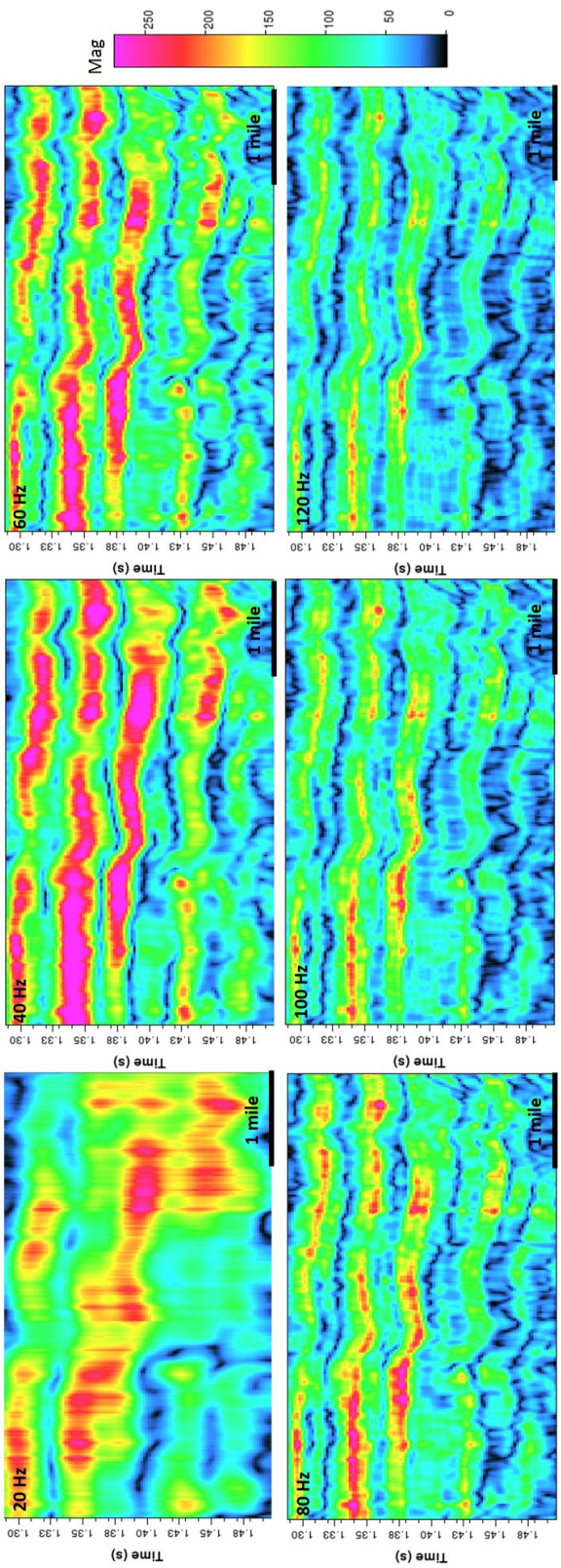

Figure 3.2. Vertical slices of spectral decompositions at frequencies 20 Hz, 40 Hz, 60 Hz, 80 Hz, 100 Hz and 120 Hz.

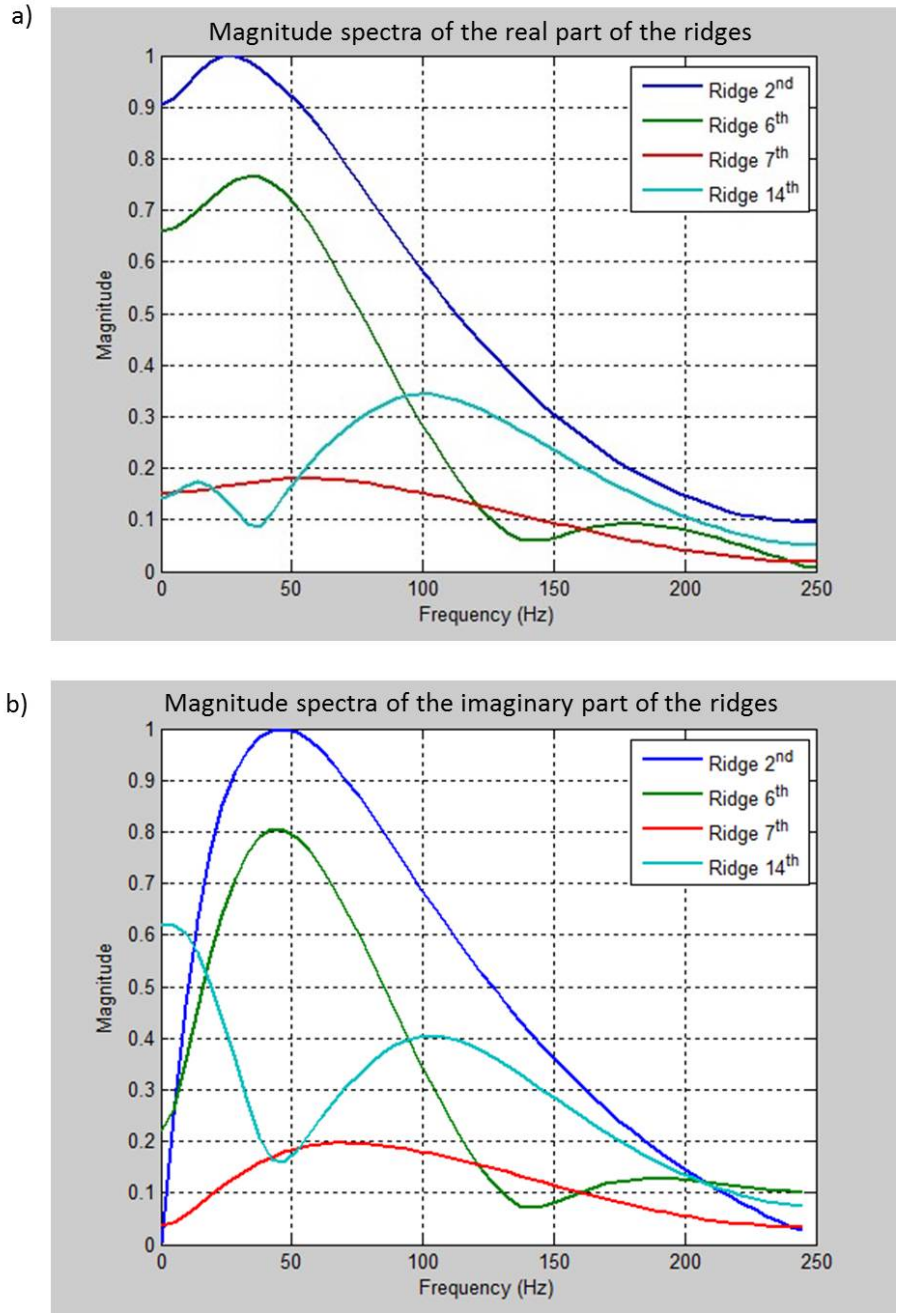

Figure 3.3. The magnitude spectra of the real and imaginary ridges that are associated with the strongest events of the signal in Figure 3.1.

workflow by convolving and summing the appropriate wavelets along the MMLs, ridge by ridge, forming a composite wavelet for each of the J ridges (3.1d and e). I then least-squares fit the J composite wavelets to the input data, forming a modeled (fit) trace, and a residual (error) trace. The standard least-squares solution to minimize the objective function $g(\mathbf{x}) = ||\mathbf{r}_k - \mathbf{M}\mathbf{x}||^2$ is given by

$$\mathbf{x} = (\mathbf{M}^T\mathbf{M} + \epsilon\mathbf{I})^{-1}\mathbf{M}^T\mathbf{r}_k, \tag{3.1}$$

where $\mathbf{x}$ is the vector that contains the coefficients of the maxima wavelets, ϵ is a small preconditioning factor and $\mathbf{I}$ is the identity matrix.

This process is repeated, with each iteration operating on the residual of the previous iteration, updating the modeled data trace until the process converges to an acceptably small residual. This algorithm has many similarities to matching pursuit (e.g. Liu and Marfurt, 2007) except that in this paper the locations of the wavelets fall along the ridges of a suite of spectral components rather than at the peak envelope of the undecomposed input or residual trace. Figure 3.5 shows the original time domain signal and its reconstruction after one to ten iterations using the real part of the maxima wavelet matrix. Figure 3.7 shows the frequency spectra of the original signal and each of the reconstruction.

Figure 3.9 shows the original time domain signal and its reconstruction after one to ten iterations using the imaginary part of the maxima wavelet matrix. Figure 3.10 shows the frequency spectra of the original signal and each of the reconstruction. Figure 3.14 shows a representative vertical line through the original seismic data and its data reconstruction after one, three and five iterations. The first iteration is Matos et al.'s (2011) ICWTD. While converging to the original data, the reconstructed data reject the steeply dipping noise.

Using the real part of the maxima wavelet matrix to reconstruct the data is better than the imaginary part because the input data is zero-phase and the real part of the maxima wavelet matrix associated with the real part of the Morlet wavelet matches with the zero-phase data better. Similarly, the imaginary part of the maxima wavelet matrix associated with the imaginary part of the Morlet wavelet is out of phase with the zero-phase data.

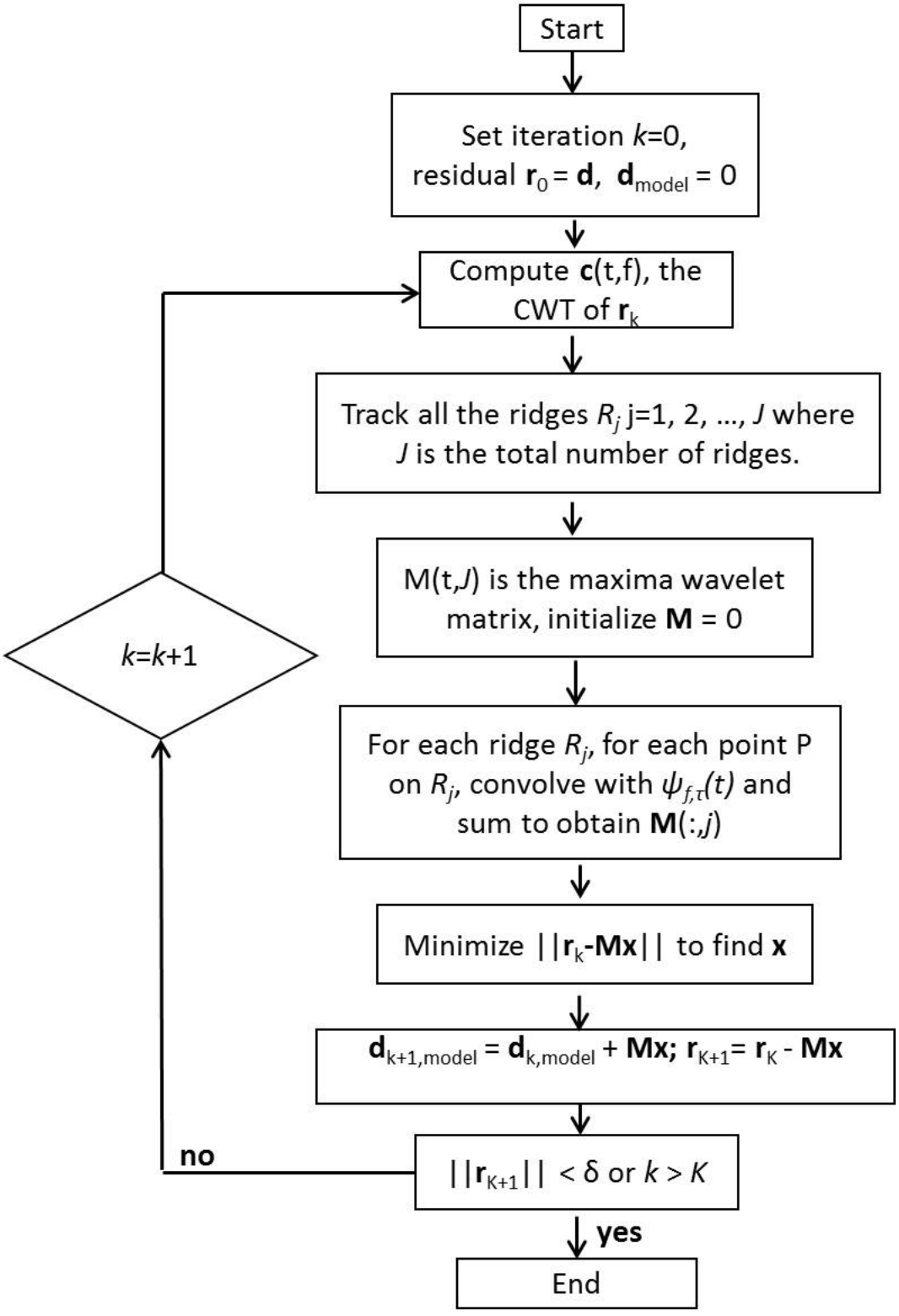

Figure 3.4. Flowchart of the matching pursuit algorithm.

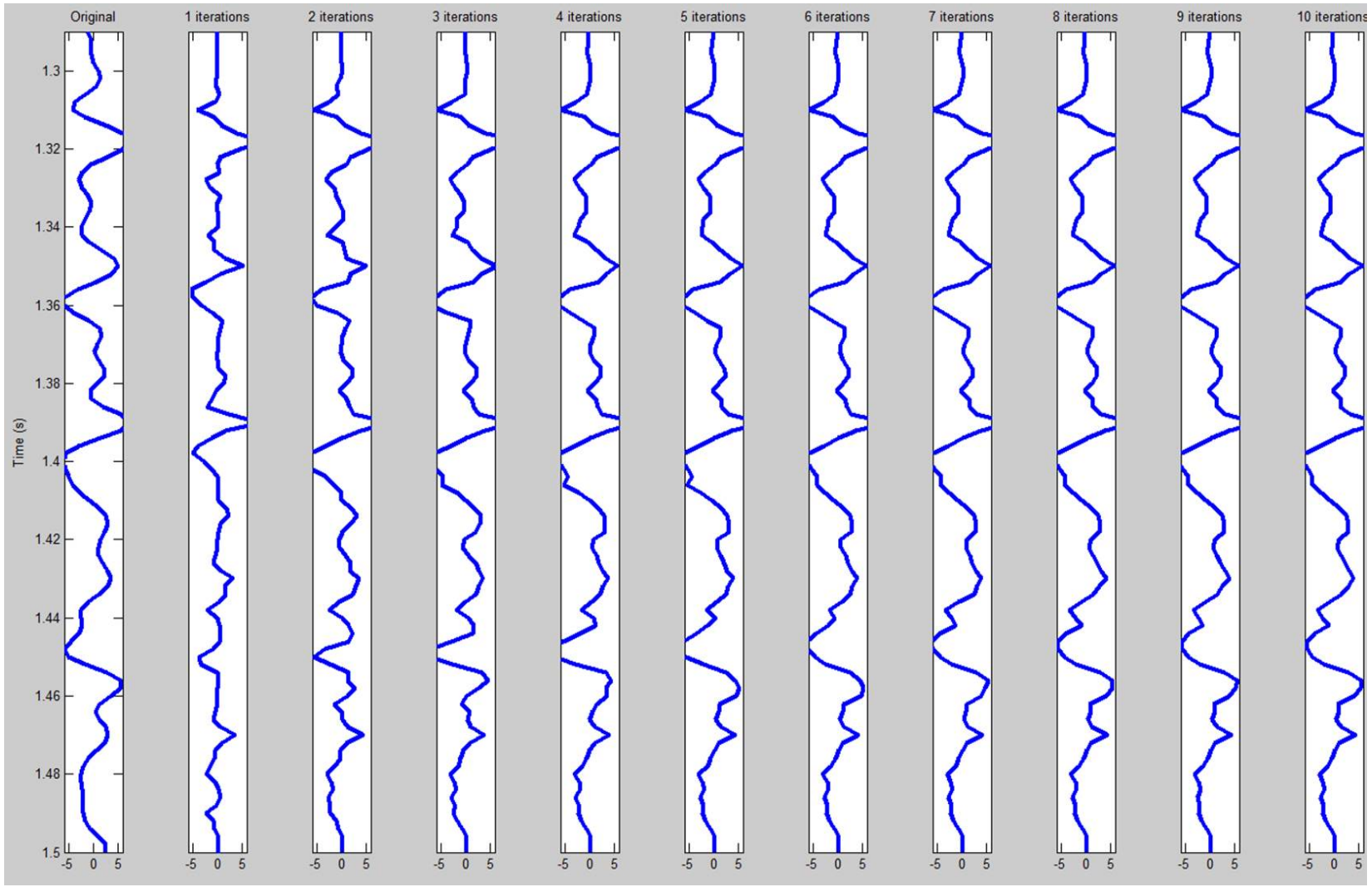

Figure 3.5. The original signal and its reconstruction after 1 through 10 iterations. The J=17 MML wavelets (the real part), $w(t)$ shown in Figure 3.1d were used for the first iteration, approximating the major characteristics and overall amplitude of the input data. The number, location, and the form of the wavelets changes with each iteration, such that the model converges to the input signal.

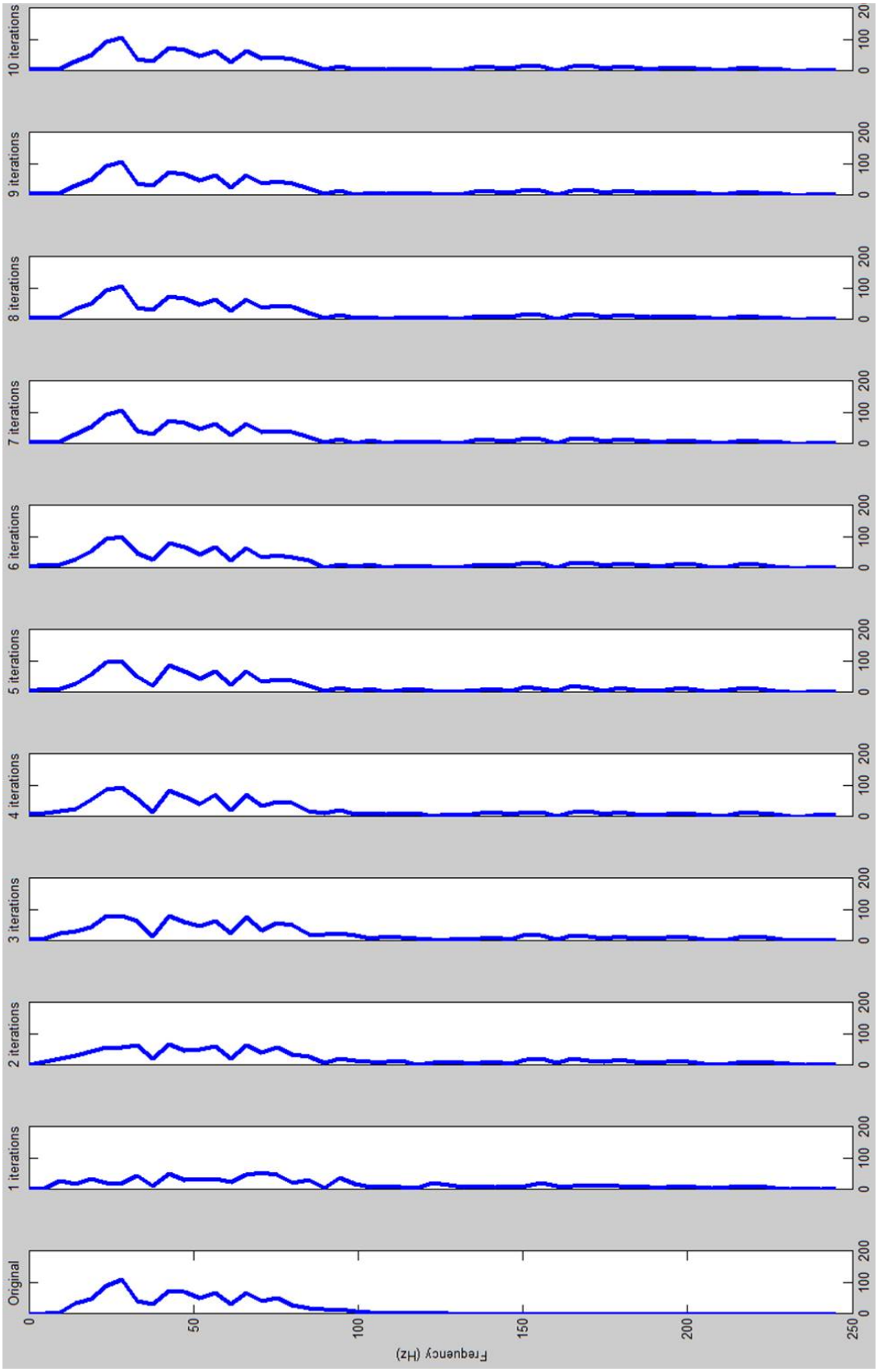

Figure 3.6. The magnitude spectra of the original signal and its reconstruction after 1 through 10 iterations using the real part of the maxima wavelets.

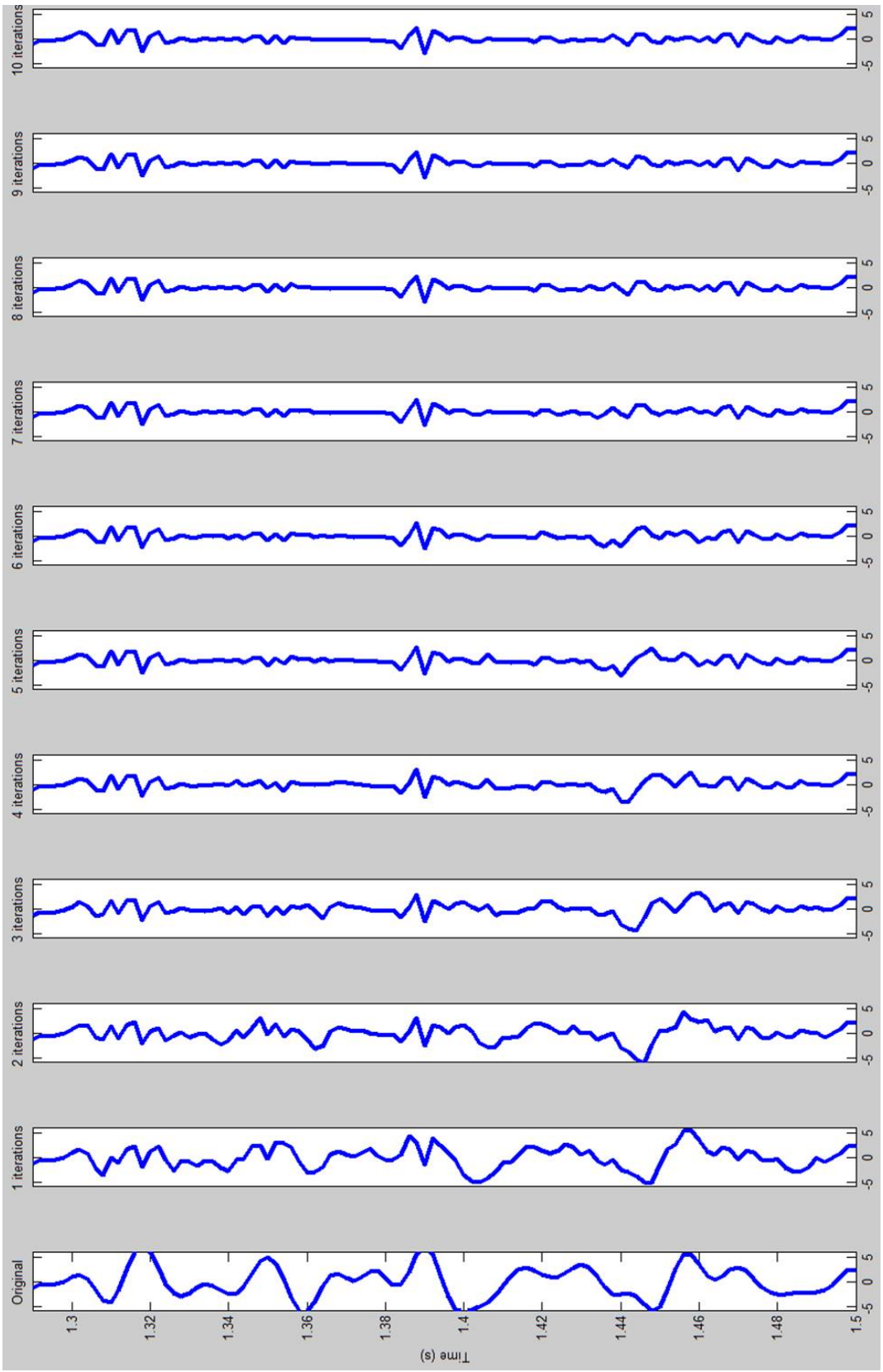

Figure 3.7. The original signal and its residual after 1 through 10 iterations.

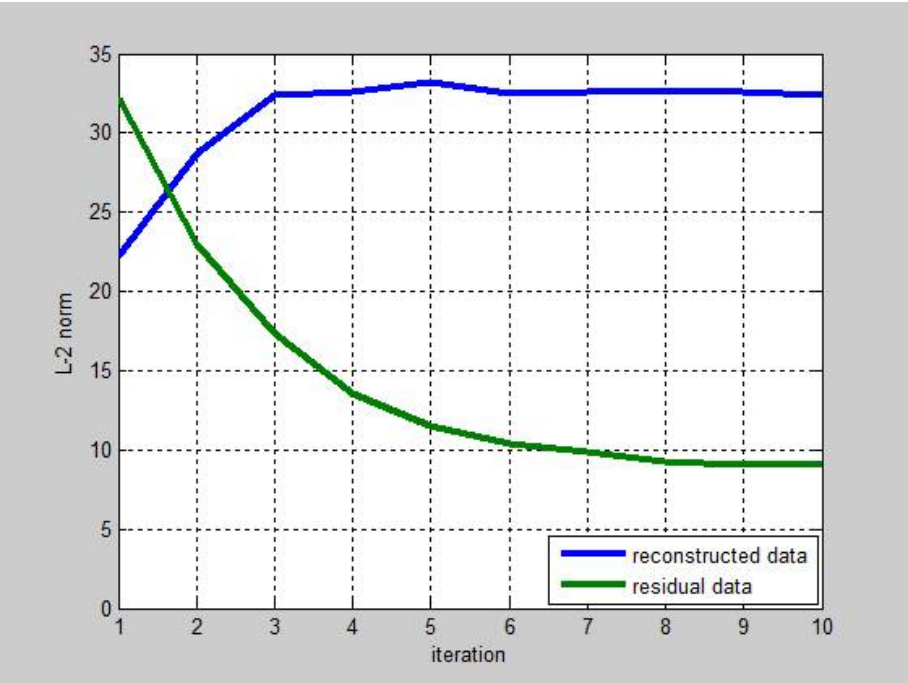

Figure 3.8. The L-2 norm of the reconstructed signals and residuals at iterations 1 through 10 using the real part of the maxima wavelet matrix.

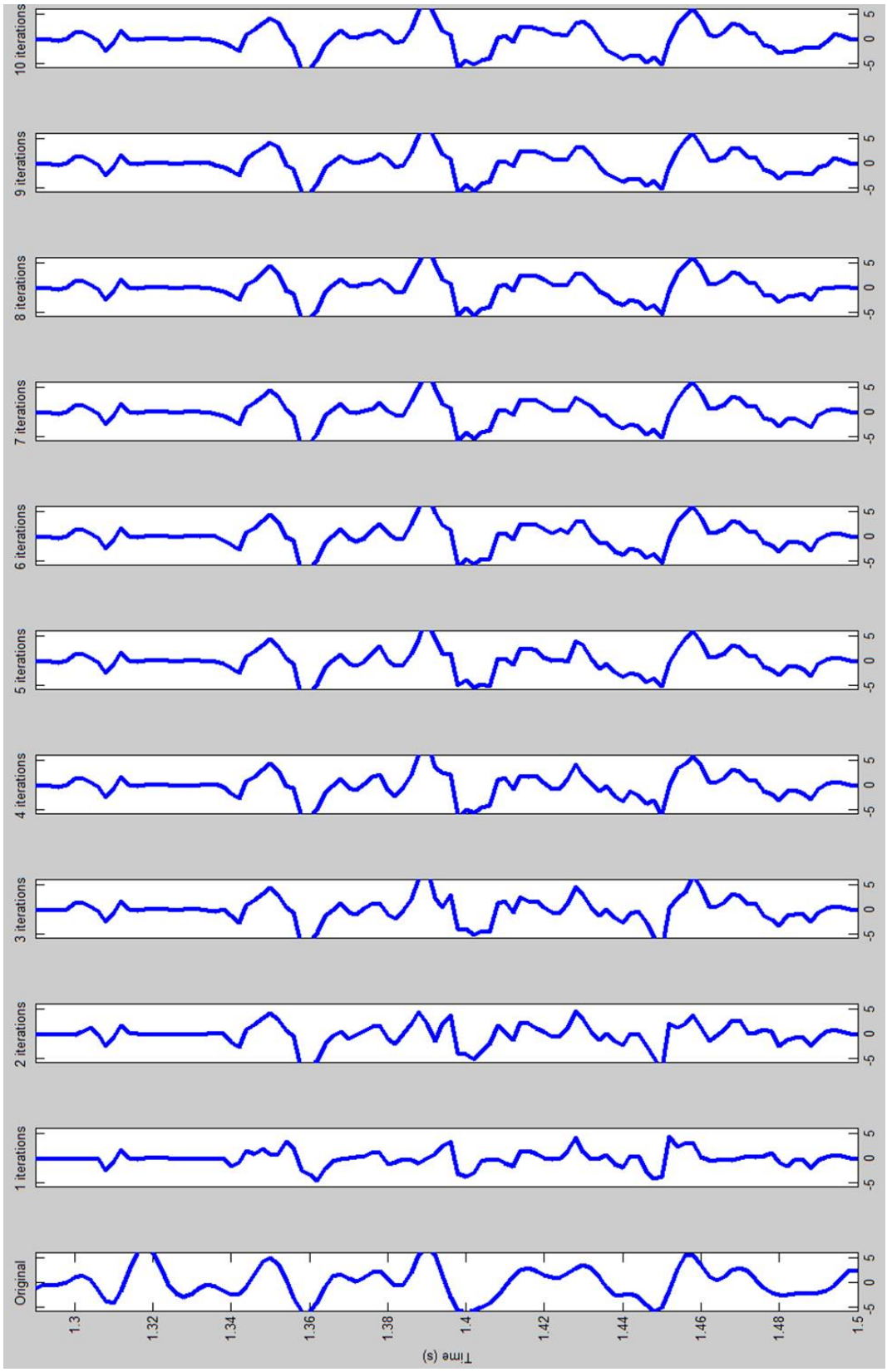

Figure 3.9. The original signal and its reconstruction after 1 through 10 iterations. The J=17 MML wavelets (the imaginary part), $w(t)$ shown in Figure 3.1e were used for the first iteration, approximating the major characteristics and overall amplitude of the input data. The number, location, and the form of the wavelets changes with each iteration, such that the model converges to the input signal.

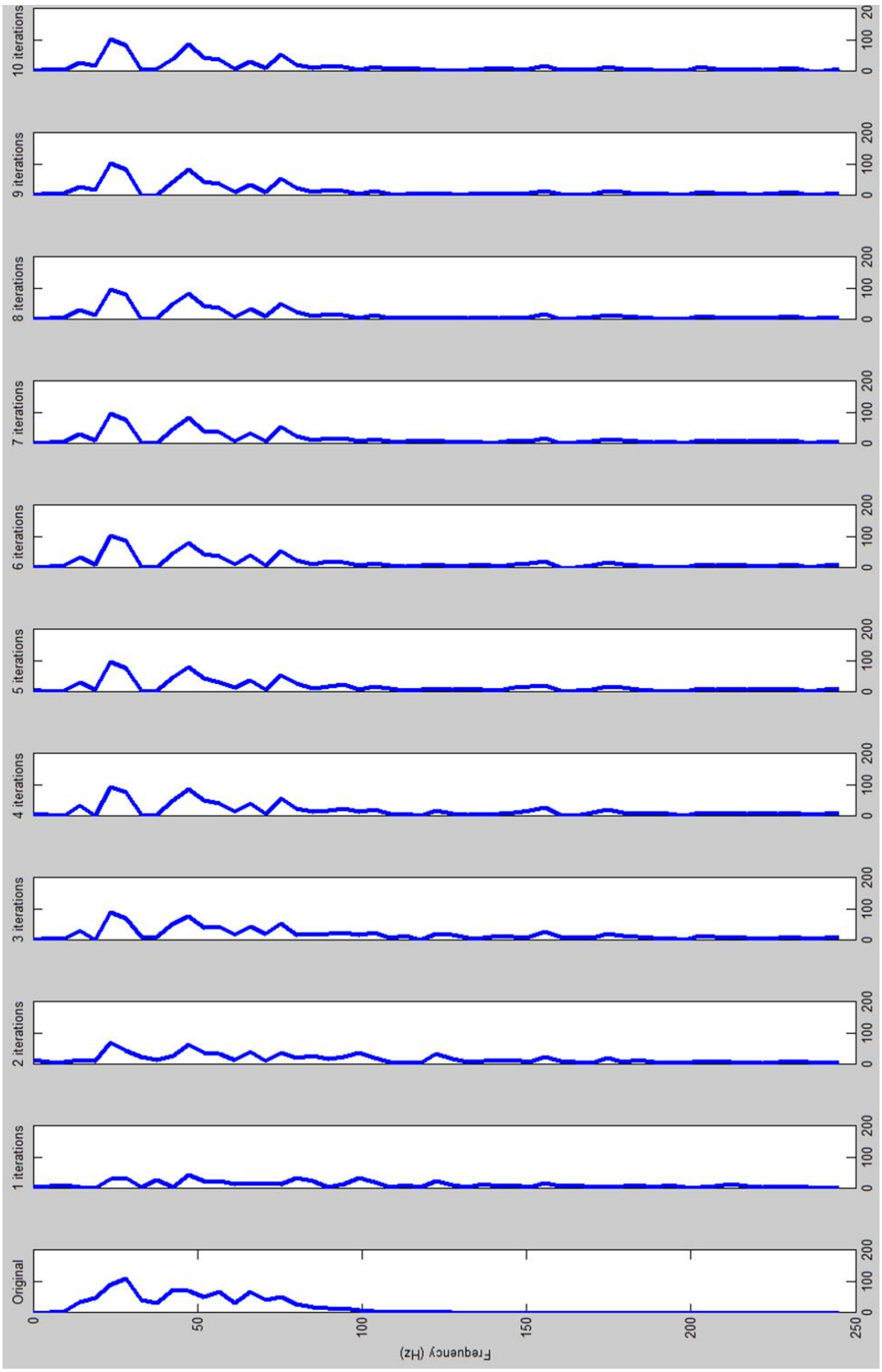

Figure 3.10. The magnitude spectra of the original signal and its reconstruction after 1 through 10 iterations using the imaginary part of the maxima wavelets.

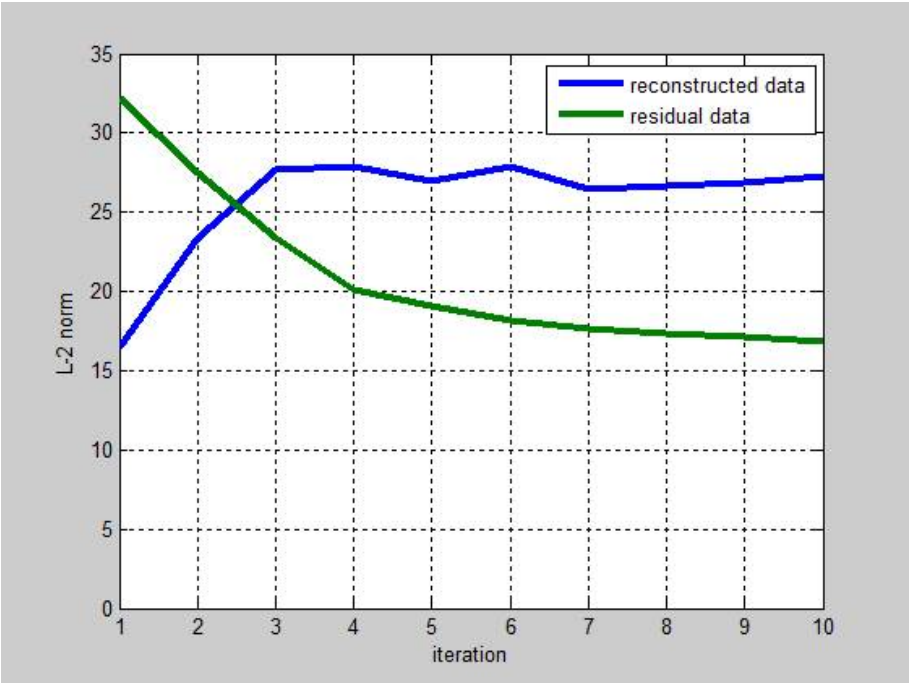

Figure 3.11. The L-2 norm of the reconstructed signals and residuals at iterations 1 through 10 using the imaginary part of the maxima wavelet matrix.

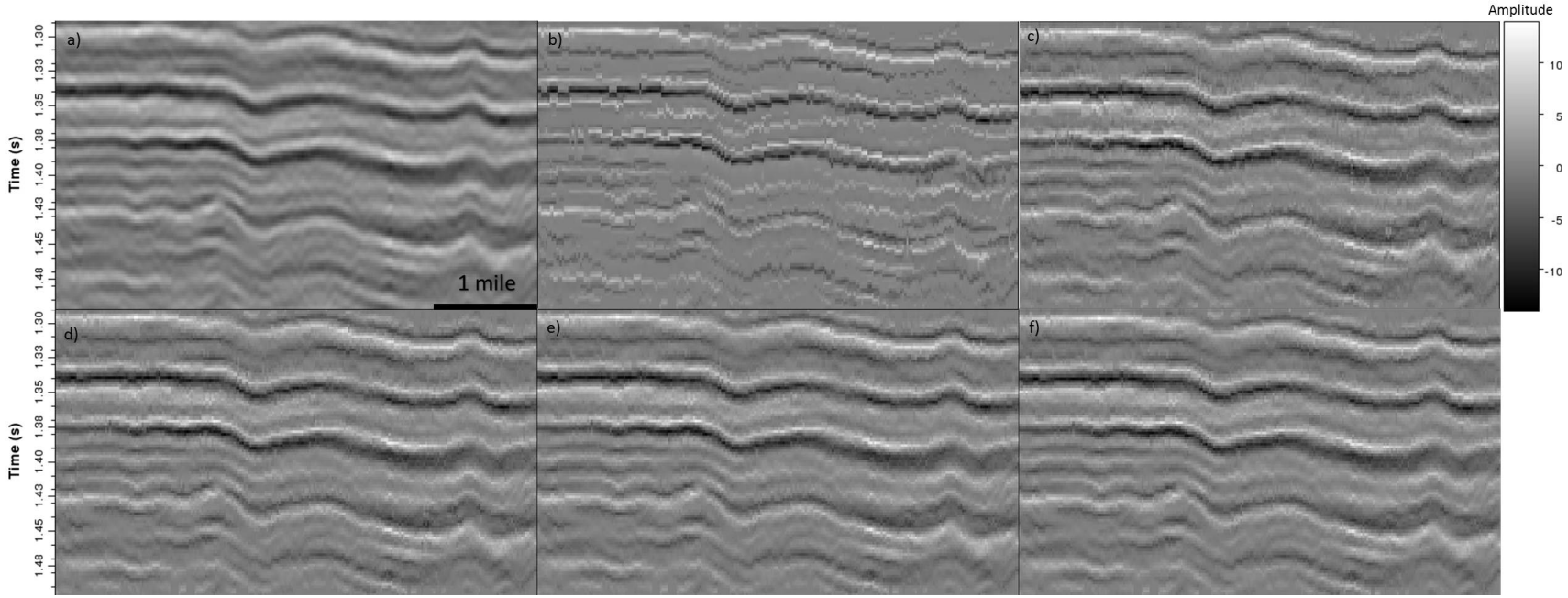

Figure 3.12. A vertical slice through (a) seismic amplitude data and the data reconstruction after (b) one, (c) three, (d) five and (e) seven and (f) nine iterations using the real part of the maxima wavelet matrix.

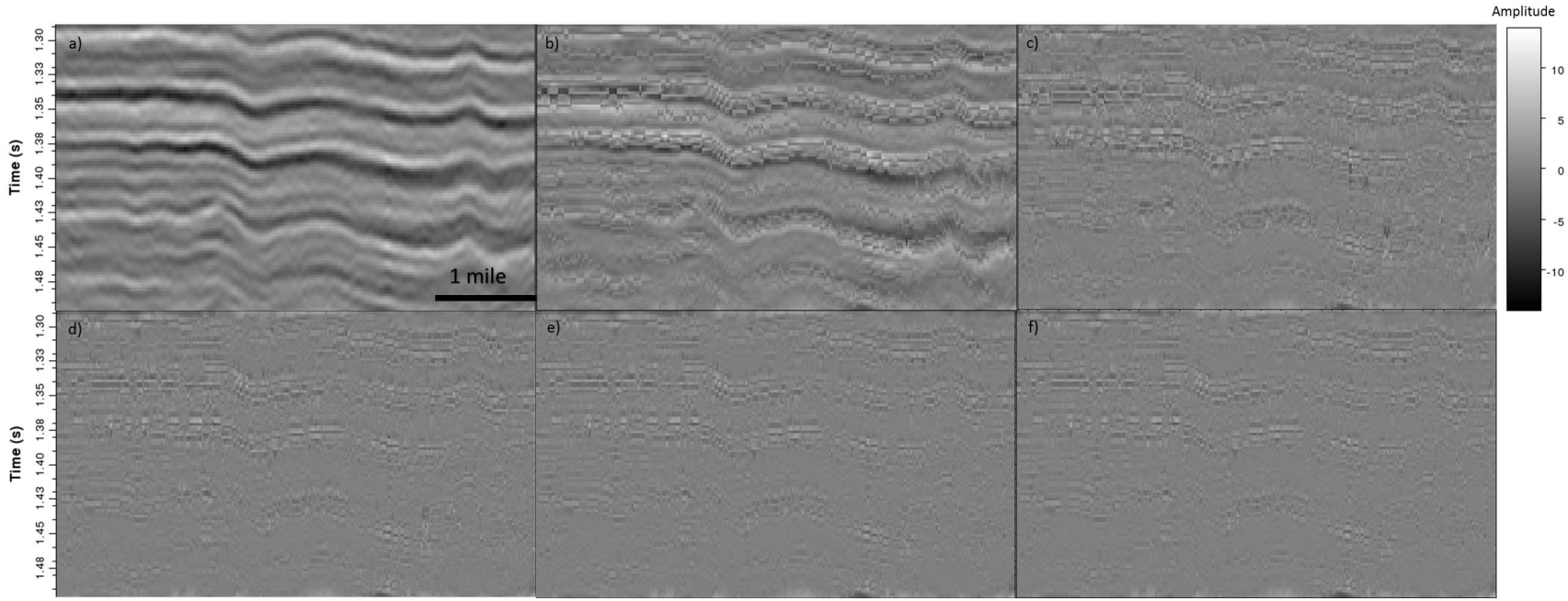

Figure 3.13. A vertical slice through (a) seismic amplitude data and the residual data after (b) one, (c) three, (d) five and (e) seven and (f) nine iterations using the real part of the maxima wavelet matrix.

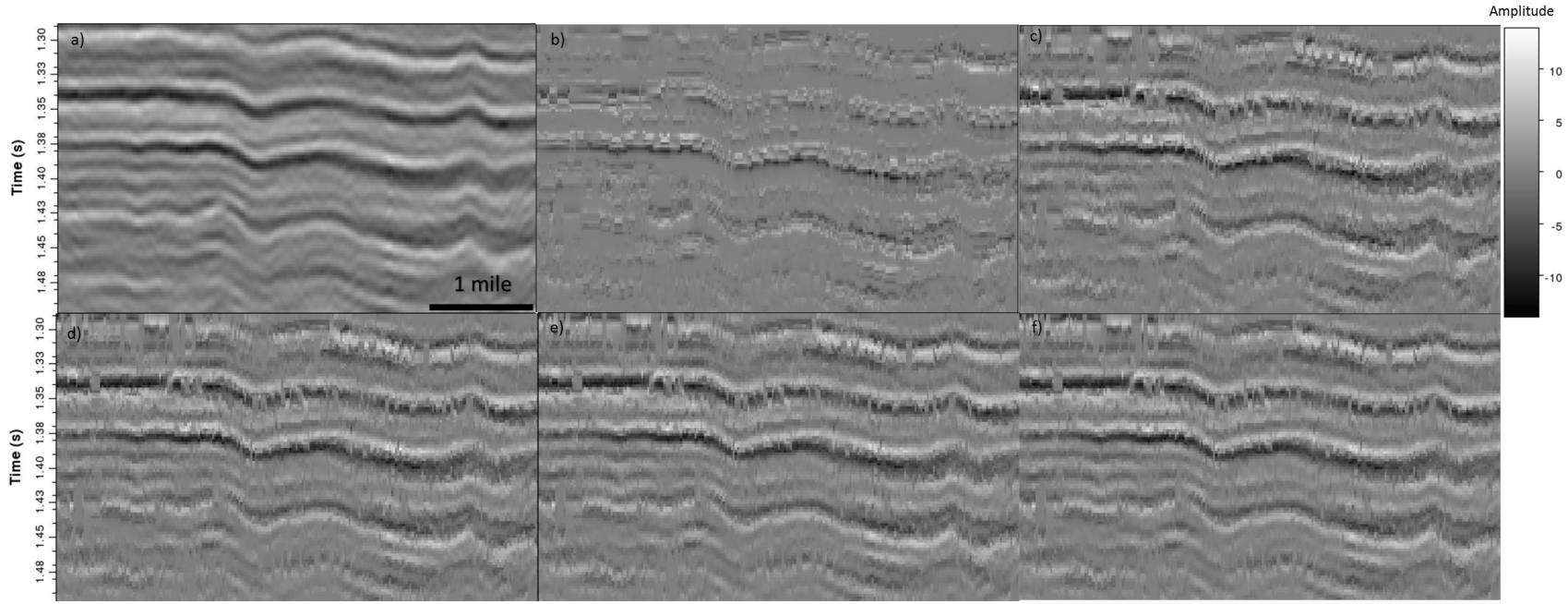

Figure 3.14. A vertical slice through (a) seismic amplitude data and the data reconstruction after (b) one, (c) three, (d) five and (e) seven and (f) nine iterations using the imaginary part of the maxima wavelet matrix.

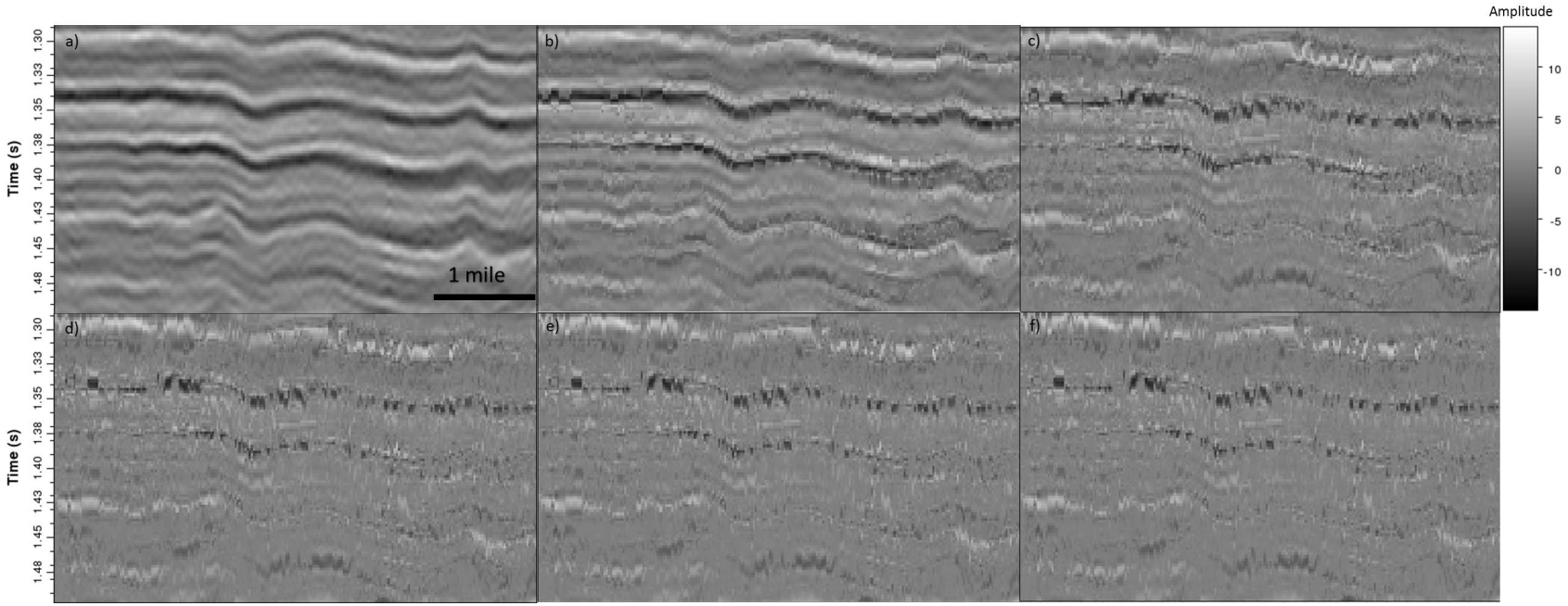

Figure 3.15. A vertical slice through a) seismic amplitude data and the residual data after (b) one, (c) three, (d) five and (e) seven and (f) nine iterations using the real part of the maxima wavelet matrix.

Chapter 4

Q ESTIMATION USING SPECTRAL DECOMPOSITION

4.1 Spectral decomposition techniques for Q estimation

The output of spectral decomposition serves as the input to estimate Q. There are as many techniques to estimate Q as methods of decomposition. Reine et al. (2009) create 1D frequency-dependent stochastic model whose $V_p = 2000\ m/s$, $\rho = 2100\ kg/m^3$, standard deviation of V_p, $\sigma_v = 7.5\%$, and standard deviation of the incompressibility fluctuations, $\sigma_k = 15\%$.

Figure 4.1 show one realization of the transmitted signal and its spectral decomposition using Short-Time window Fourier Transform, the Gabor transform, the S-transform and the Continuous Wavelet Transform. Figure 4.2a shows the frequency-dependent Q of the realization in Figure 4.1.

20 realizations of the model are generated and decomposed into frequency bands using four different methods. Figure 4.2b shows the theoretical and mean measured $1/Q$ profiles. From the experiments, Reine et al. (2009) conclude that the attenuation measurements made by variable-window continuous wavelet transform and S-transform are both more stable and give stronger match to the model than the fixed window Fourier Transform. Based on this result, I will attempt to compute Q using the Continuous Wavelet Transform technique that I develop in Chapter 3.

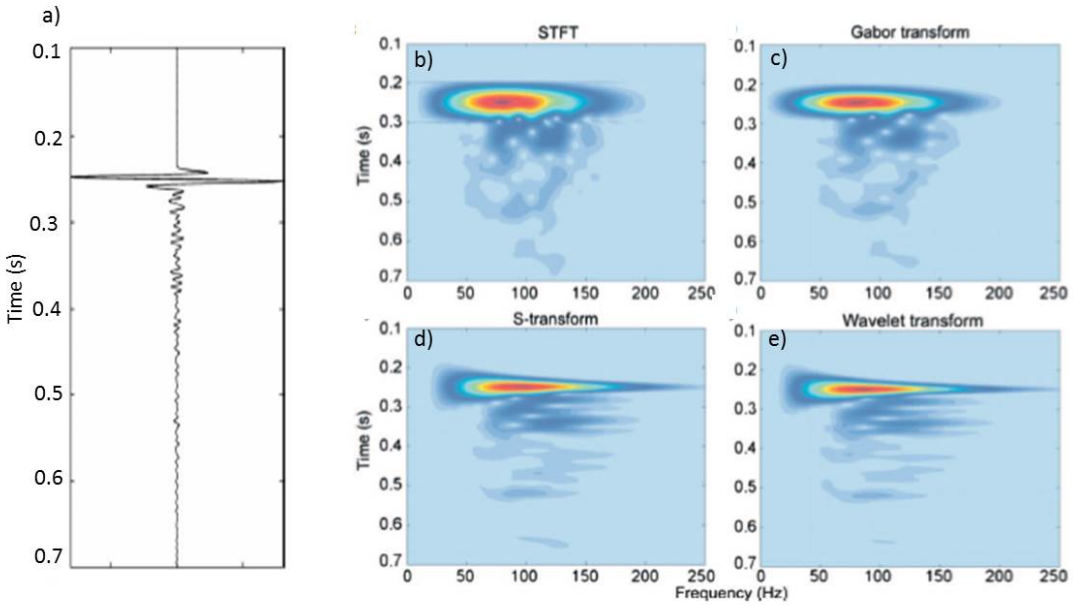

Figure 4.1. (a) A single realization of the P-wave velocity and its corresponding seismic signal, the spectra of the signal using (b) Short-Time Fourier Transform, (c) Gabor transform, (d) S-transform and (e) Continuous Wavelet Transform (After Reine et al., 2009).

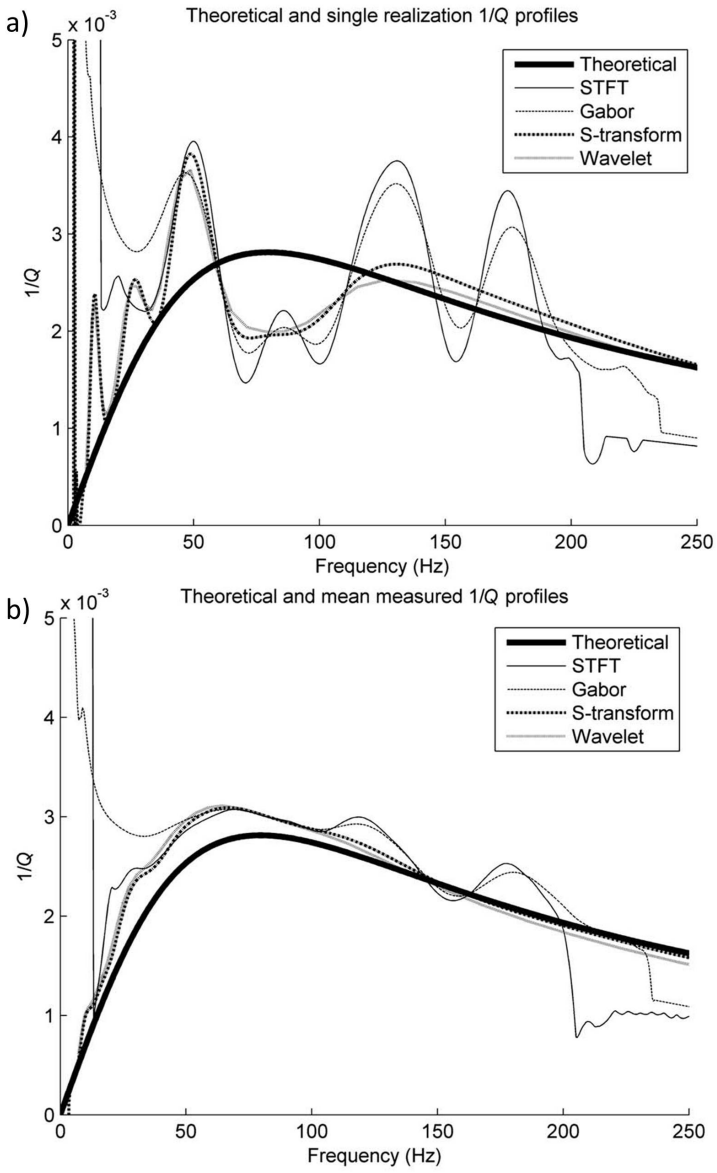

Figure 4.2. The theoretical and estimated Q of (a) the realization plotted in Figure 4.1 and (b) the mean of 20 realizations using four different spectral decomposition techniques. The variable-window transforms have a better and stable match to the models (After Reine et al., 2009).

4.2 Data pre-conditioning

The target area is contaminated with the steeply dipping high frequency noise which I interpret to be migration operator aliasing. Before estimating Q, I apply structure-oriented filter (SOF) to the data. Figure 4.3a shows a representative vertical slice through the original prestack time migrated seismic amplitude volume. Figure 4.3b shows the same slice after two passes of structure-oriented filtering using a 110 by 110 ft circular 5-trace window by 10 ms (11 samples). Much of the high-frequency dipping noise cutting across the relatively flat has been rejected. Figure 4.3c shows the rejected noise computed by subtracting the data shown in Figure 4.3b from that shown in Figure 4.3a. Note that the rejected noise is higher frequency but spatially chaotic and not correlated to geology. Figures 4.4 show a representative time slice at $t = 1.3$ s through the original seismic amplitude data, the filtered data and the rejected noise. Note that the short wavelength "checkboard" noise cutting across the relatively flat reflectors that correspond to the migration aliasing artifacts seen previously in Figure 4.3a is filtered out.

The structure-oriented filtered seismic amplitude data shown in 4.3b are then spectrally whitening within a 5-130 Hz window, with a preconditioning of 4%. Figures 4.5 show a representative time slice through the original prestack time migrated seismic amplitude volume and the seismic amplitude data after two passes of SOF and spectral whitening. The white arrows indicate thin reflectors in the target area that are better resolved. Figures 4.6 show vertical slices through spectral components at 20, 40, 60, 80, 100, and 120 Hz computed from the data shown in Figure 4.5b after two passes of SOF and spectral balancing. Note that the frequency response is similar in the 20-100 Hz range but falls off at

120 Hz. Figures 4.7 show time slices at t=1.3 s through the spectral magnitude components at 20, 40, 60, 80, 100, and 120 Hz computed from the data shown in Figure 4.4b after SOF and spectral balancing. Figures 4.8 show horizons slices along the top Lower Barnett Shale horizon through spectral magnitude components at 20, 40, 60, 80, 100, and 120 Hz.

4.3 Principal Component Analysis

Seismic data are noisy such that we need to condition our data before using the Q estimation methods I introduced in chapter 2. First, I need to interpolate the complex spectra along user defined surfaces. Specifically, I interpolate real and imaginary components along a suite of stratal slices (Appendix C). Next I filter the spectra of the two surfaces using Principal Component Analysis, an orthogonal linear transformation that estimates the correlation between measurements. There are a number of methods to implement the PCA algorithm. In this thesis, I use the one described by Guo et al. (2009), which is summarized in Appendix B.

Given the spectra of a data volume, each frequency component represents a measurement. The measurements are normalized to zero-mean, then input to the PCA algorithm. If the spectra along a given horizon or stratal slice have the same shape, they will be completely defined by the first eigenspectrum. Eigenspectra that are associated with second, third, forth, and so on largest eigenvalues reveal variations in the spectra that are critical to the Q estimation algorithm.

Figure 4.10 shows the real and the imaginary parts of the first five eigenspectra of the covariance matrices computed along the top of the Lower Barnett

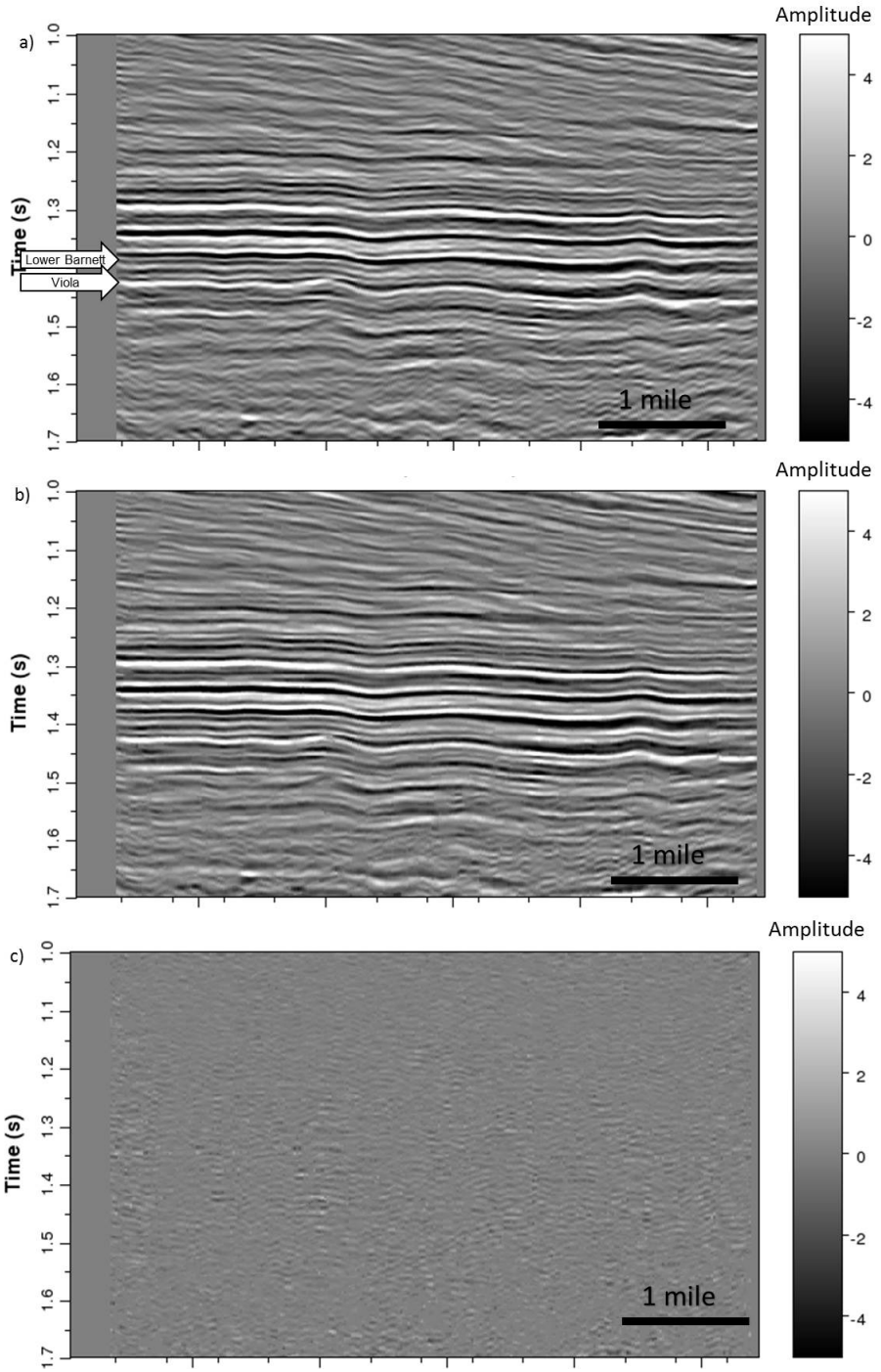

Figure 4.3. A representative vertical slice through (a) the original prestack time migrated seismic amplitude volume, (b) the seismic amplitude data after two passes of structure-oriented filtering using a 110 by 110 ft circular 5-trace window by 10 ms (11 samples) and (c) the rejected noise volume computed by subtracting the data shown in Figure 4.3b from that shown in Figure 4.3a.

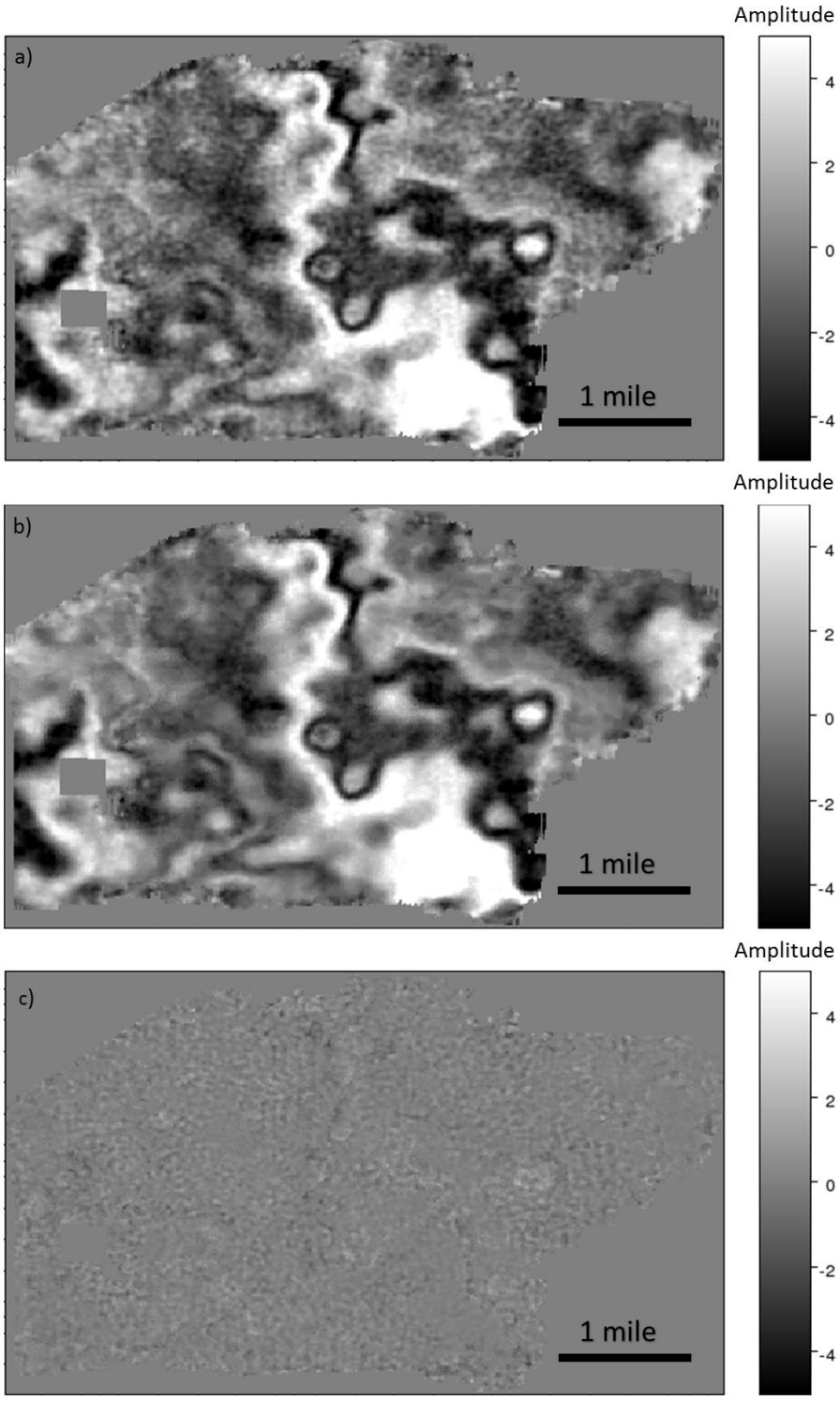

Figure 4.4. A representative time slice through (a) the original prestack time migrated seismic amplitude volume, (b) the seismic amplitude data after two passes of SOF and (c) the rejected noise volume computed by subtracting the data shown in Figure 4.4b from that shown in Figure 4.4a.

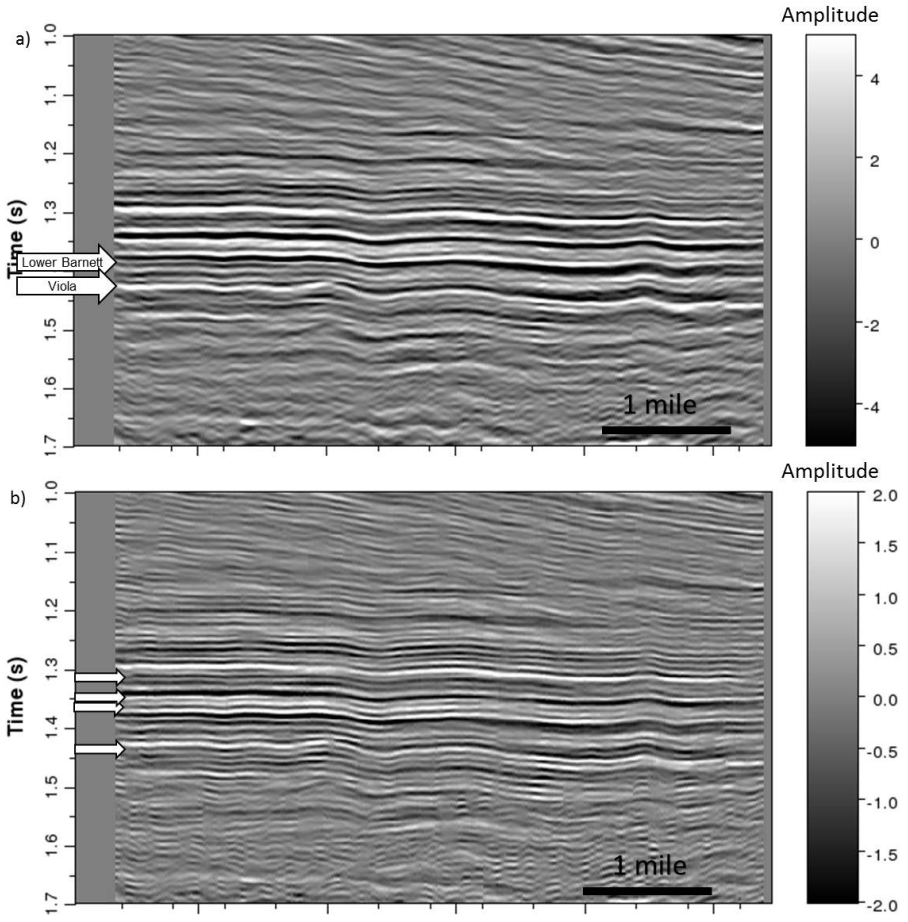

Figure 4.5. A representative time slice through (a) the original prestack time migrated seismic amplitude volume and (b) the seismic amplitude data after two passes of SOF and spectral whitening.

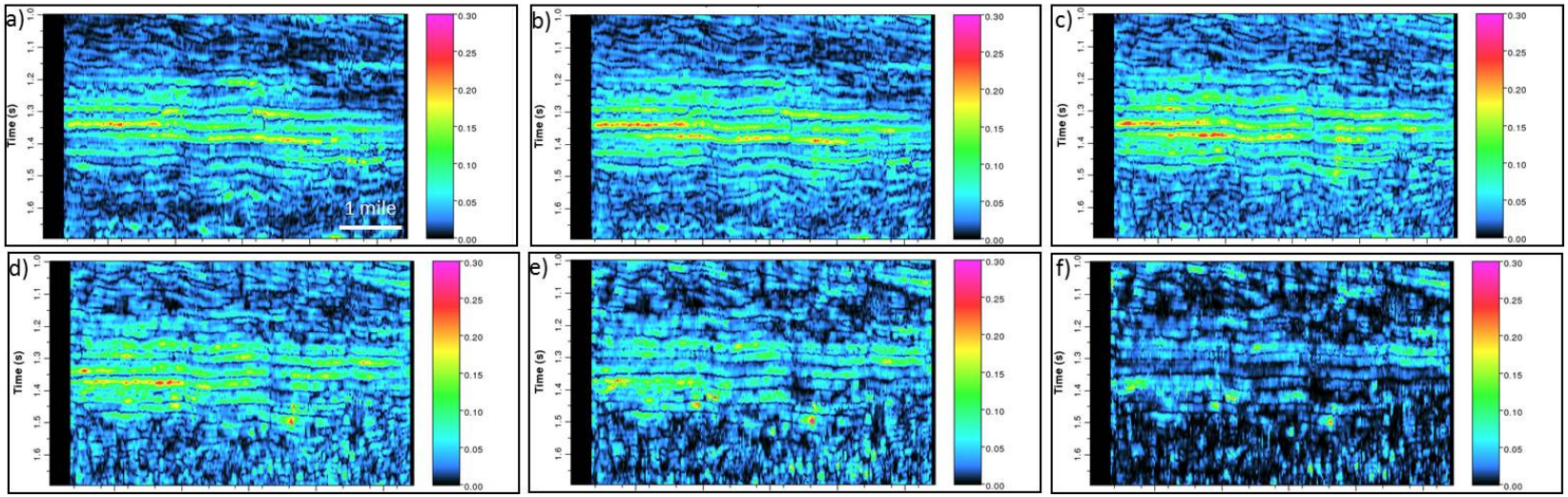

Figure 4.6. Vertical slices through spectral components at (a) 20, (b) 40, (c) 60, (d) 80, (e) 100, and (f) 120 Hz computed from the data shown in Figure 4.5b after two passes of SOF and spectral balancing. Note that the frequency response is similar in the 20-100 Hz range but falls off at 120 Hz.

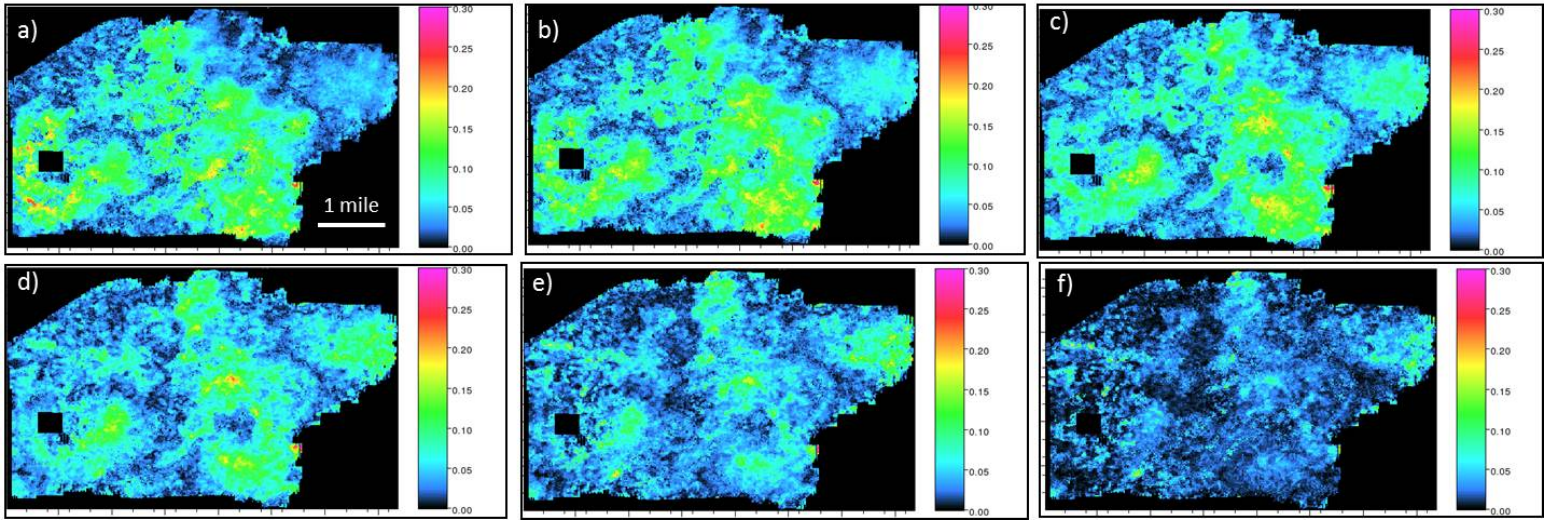

Figure 4.7. Time slices at t=1.3 s through the spectral magnitude components at (a) 20, (b) 40, (c) 60, (d) 80, (e) 100, and (f) 120 Hz computed from the data shown in Figure 4.4b after SOF and spectral balancing.

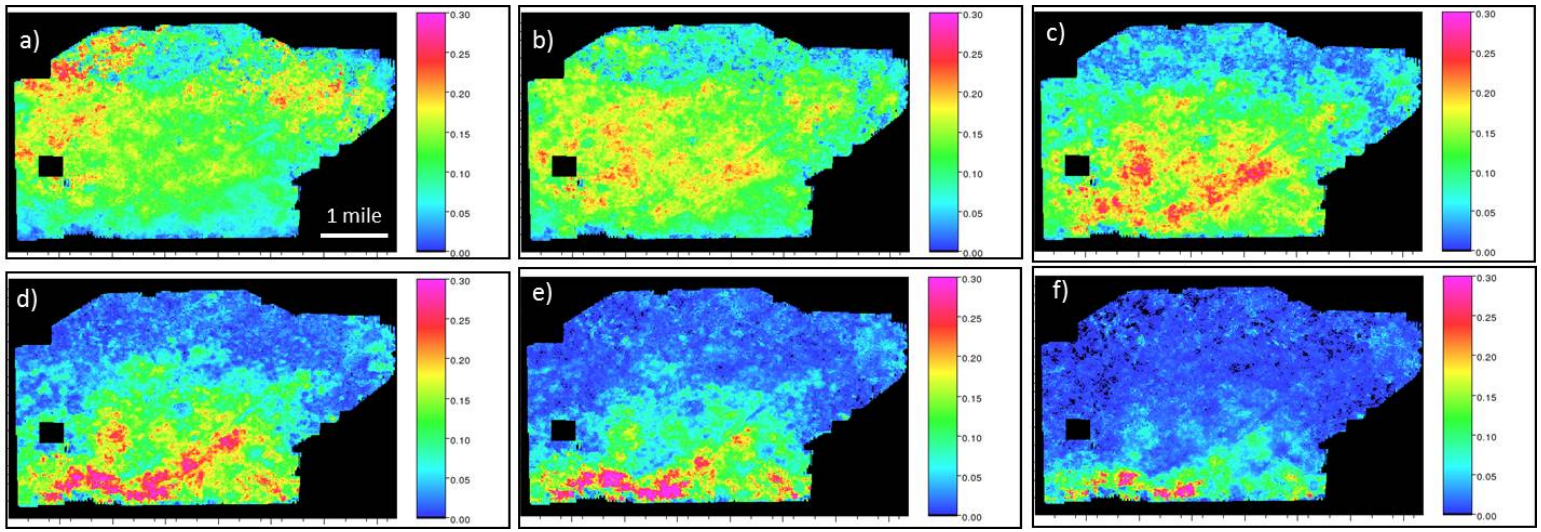

Figure 4.8. Horizons slices along the top Lower Barnett Shale horizon through spectral magnitude components at (a) 20, (b) 40, (c) 60, (d) 80, (e) 100, and (f) 120 Hz.

Shale and the Viola Limestone. Figure 4.9 shows the first ten normalized eigenvalues of the covariance matrices corresponding to the two surfaces. In the Lower Barnett Shale, 78.7%, 18.8% and 2.08% of the data can be represented by the first, second and the third eigenspectra, respectively. The remaining 21 eigenspectra represent only 0.42% of the variability of the data. Similarly, in the Viola Limestone, the first eigenspectra represents 85.3%, the second eigenspectra represents 11.8% of the data and the third eigenspectra represents 2.46% of the data. The remaining 21 eigenspectra represent only 0.44% of the data variability. For this reason, I only use the first two eigenspectra to represent the spectra of all the traces used in the computation of the covariance matrix. If the geology is structurally complex, the spectra will change rapidly along time slices and will require more eigenspectra to express the variation.

Figure 4.10 shows the first four eigenvectors calculated along the top of the Lower Barnett Shale and the Viola Limestone after two passes of structured-oriented filter and spectral balancing. Figures 4.11 and 4.12 show the horizon slices along the two surfaces through spectral magnitude component at 20, 40, 60, 80, 100, and 120 Hz after principal component filtering using the first three of 24 eigenspectra.

4.4 Q estimation using the spectral ratio method

To estimate Q, I minimize the objective function with respect to $\frac{1}{Q}$ and m

$$\chi(Q) = \sum_{j=1}^{N} a_1(f_j)a_2(f_j)\left[\ln\frac{a_2(f_j)}{a_1(f_j)} + \frac{\pi f_j \Delta t}{Q} - m\right]^2, \tag{4.1}$$

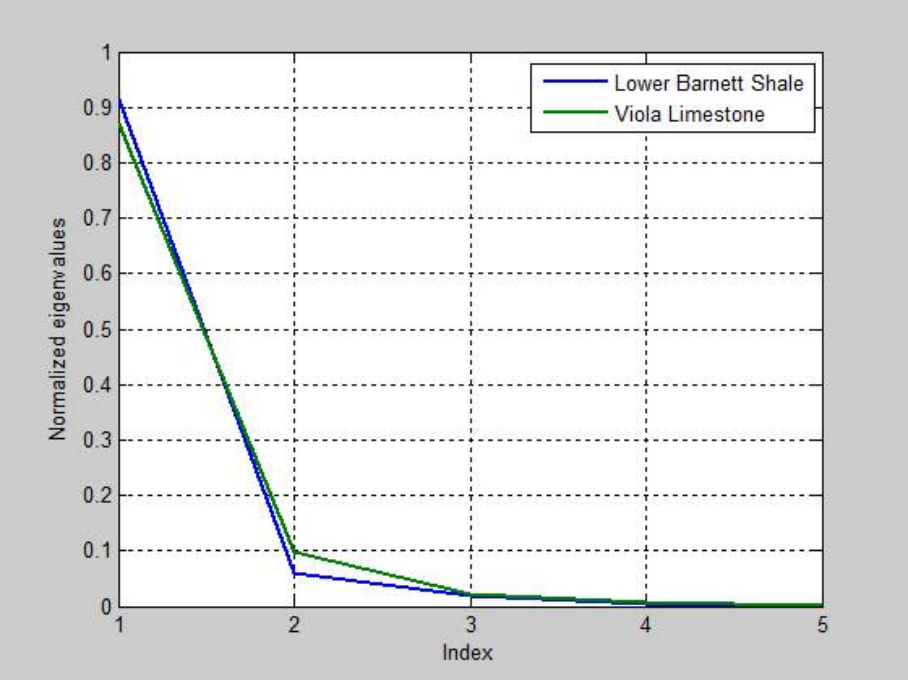

Figure 4.9. First five normalized eigenvalues of the covariance matrix corresponding to the top of the Lower Barnett Shale and the Viola Limestone.

where $a_1(f_j)$ and $a_2(f_j)$ are given by the filtered spectral decomposition data and m is the unknown intercept value. The products $a_1(f_j)a_2(f_j)$ weight the importance of the spectral ratio at frequency f_j.

Equation 4.1 can be rewritten in the form

$$\chi(Q) = (\mathbf{Ax} - \mathbf{b})^T \mathbf{W}(\mathbf{Ax} - \mathbf{b}), \tag{4.2}$$

where the matrix

$$\mathbf{A} = \begin{bmatrix} f_1 & f_2 & \cdots & f_n \\ 1 & 1 & \cdots & 1 \end{bmatrix}^T, \tag{4.3}$$

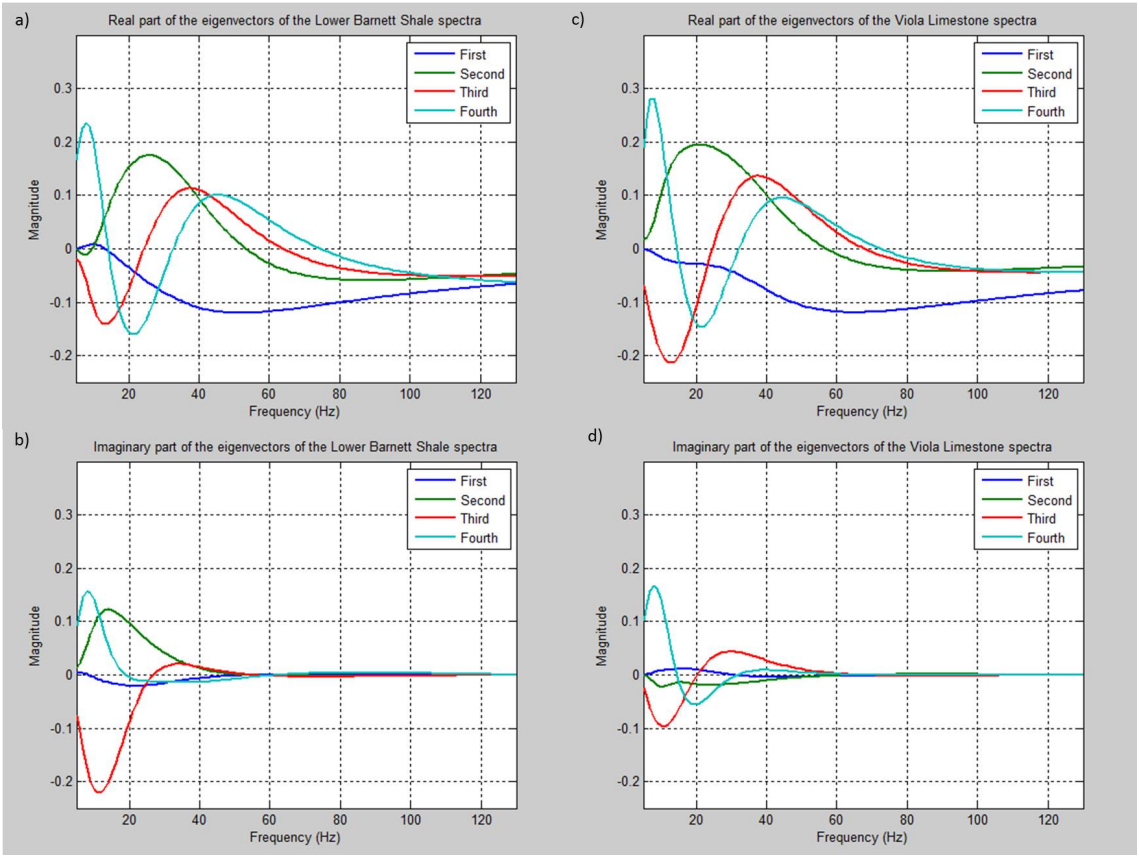

Figure 4.10. The real and imaginary parts of the first four eigenvectors calculated along the top of the (a), (b) Lower Barnett Shale and (c), (d) the Viola Limestone after two passes of SOF and spectral balancing.

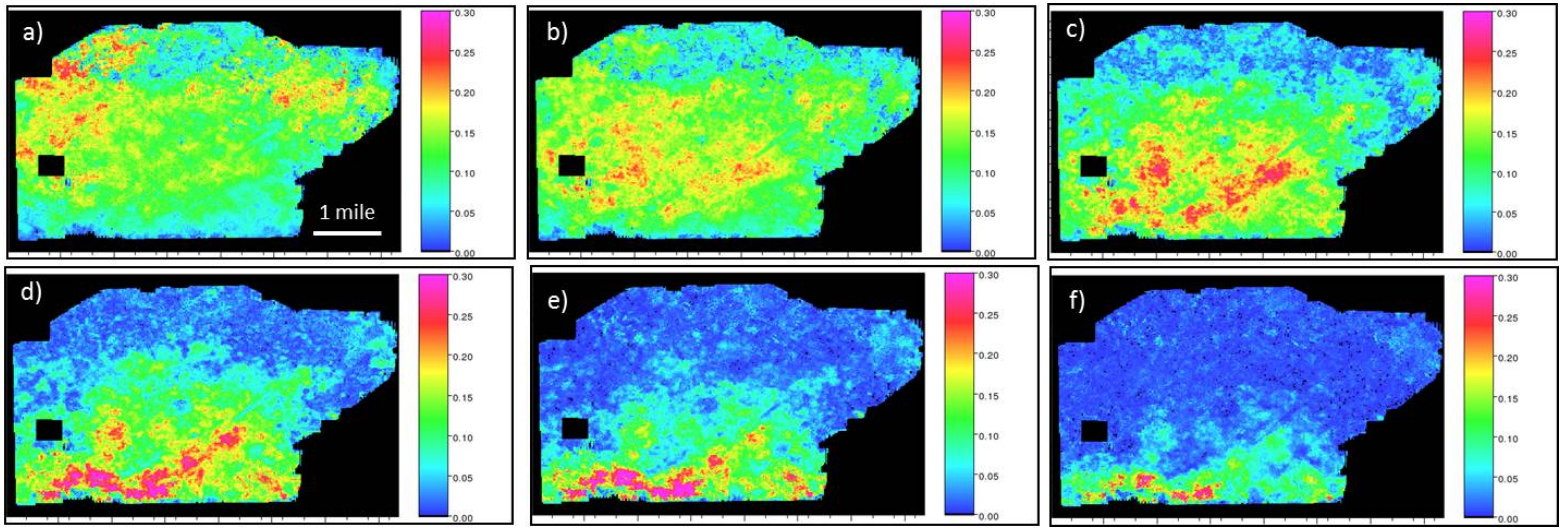

Figure 4.11. Horizons slices along the top Lower Barnett Shale horizon through spectral magnitude components at 20, 40, 60, 80, 100, and 120 Hz after principal component filtering using the first three of 24 eigenspectra.

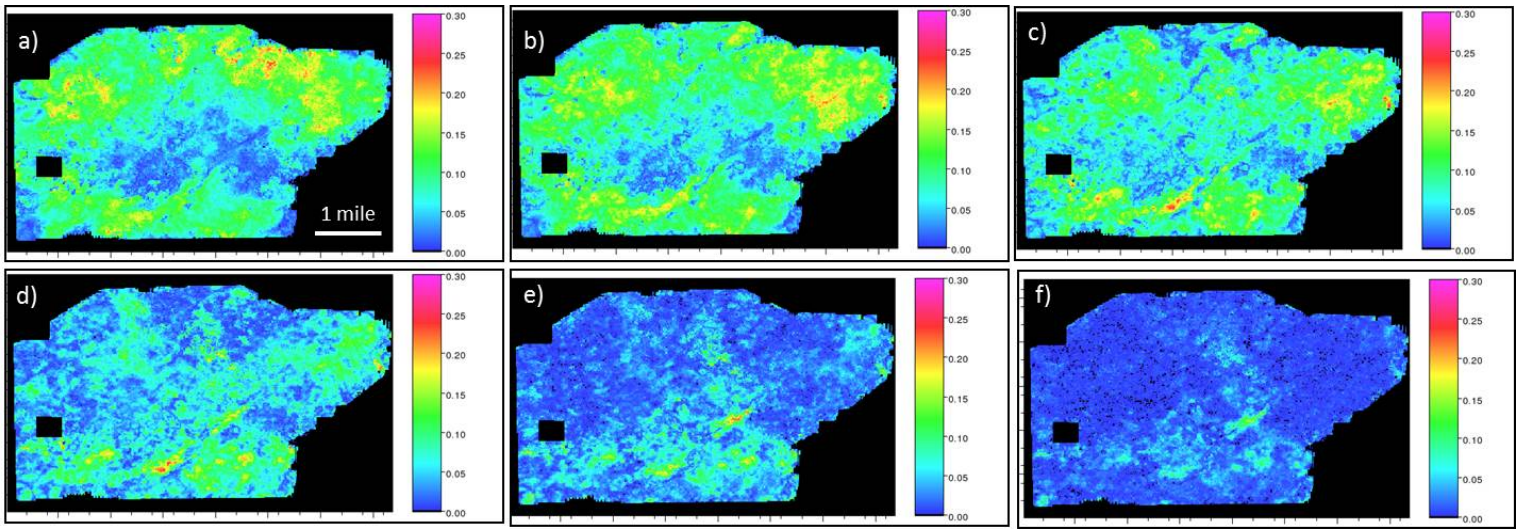

Figure 4.12. Horizons slices along the top Viola Limestone horizon through spectral magnitude components at 20, 40, 60, 80, 100, and 120 Hz after principal component filtering using the first three of 24 eigenspectra.

the weight matrix $\mathbf{W}$ is an N by N diagonal matrix

$$\mathbf{W} = \begin{bmatrix} a_1(f_1)a_2(f_1) & & & \\ & a_1(f_2)a_2(f_2) & & \\ & & \ddots & \\ & & & a_1(f_N)a_2(f_N) \end{bmatrix}, \tag{4.4}$$

the vector

$$\mathbf{b} = \begin{bmatrix} \ln \frac{a_2(f_1)}{a_1(f_1)} & \ln \frac{a_2(f_2)}{a_1(f_2)} & \cdots & \ln \frac{a_2(f_n)}{a_1(f_n)} \end{bmatrix}^T, \tag{4.5}$$

and the unknown vector

$$\mathbf{x} = \begin{bmatrix} -\frac{\pi \Delta t}{Q} & m \end{bmatrix}^T. \tag{4.6}$$

The standard weighted least squares solution is

$$\mathbf{x_w} = (\mathbf{A}^T \mathbf{W} \mathbf{A})^{-1} \mathbf{W} \mathbf{A}^T \mathbf{b}. \tag{4.7}$$

To enhance the stability of the solution, I solve this optimization problem using iteratively re-weighted least squares to remove outliners. The residual $\mathbf{r}$ is given by

$$\mathbf{r} = \mathbf{b} - \mathbf{A}\mathbf{x_w}. \tag{4.8}$$

The new weight matrix $\widetilde{\mathbf{W}}$ is an N by N diagonal matrix:

$$\widetilde{\mathbf{W}} = \begin{bmatrix} \frac{1}{1+|r_1|^2} & & & \\ & \frac{1}{1+|r_2|^2} & & \\ & & \ddots & \\ & & & \frac{1}{1+|r_N|^2} \end{bmatrix}. \tag{4.9}$$

Minimizing the objective function but now with the weight $\widetilde{\mathbf{W}}$, the solution is

$$\widetilde{\mathbf{x}} = (\mathbf{A}^T\widetilde{\mathbf{W}}\mathbf{A})^{-1}\widetilde{\mathbf{W}}\mathbf{A}^T\mathbf{b}. \tag{4.10}$$

Figure 4.13 shows the filtered normalized spectra at two representative points on the top of lower Barnett Shale and Viola Limestone.

4.5 Application and Discussion

Figure 4.14a shows a vertical slice of the seismic amplitude data rendered with the time structure maps of the top of the Lower Barnett Shale and the Viola Limestone. Figure 4.15 shows the computed Q map. The estimated Q values are not correct due to a number of factors. In terms of processing, accurate Q values require very careful processing workflow that do not dramatically alter the frequency content of the data. In particular, stretch due to migration algorithms introduces a distortion of the resulting spectrum. If the picked velocity is too fast or too slow, the imaged reflector will be under or over corrected. After stack high frequencies will be attenuated, while low frequencies will be preserved. My data were stacked by a commercial processor so I have no quality control over

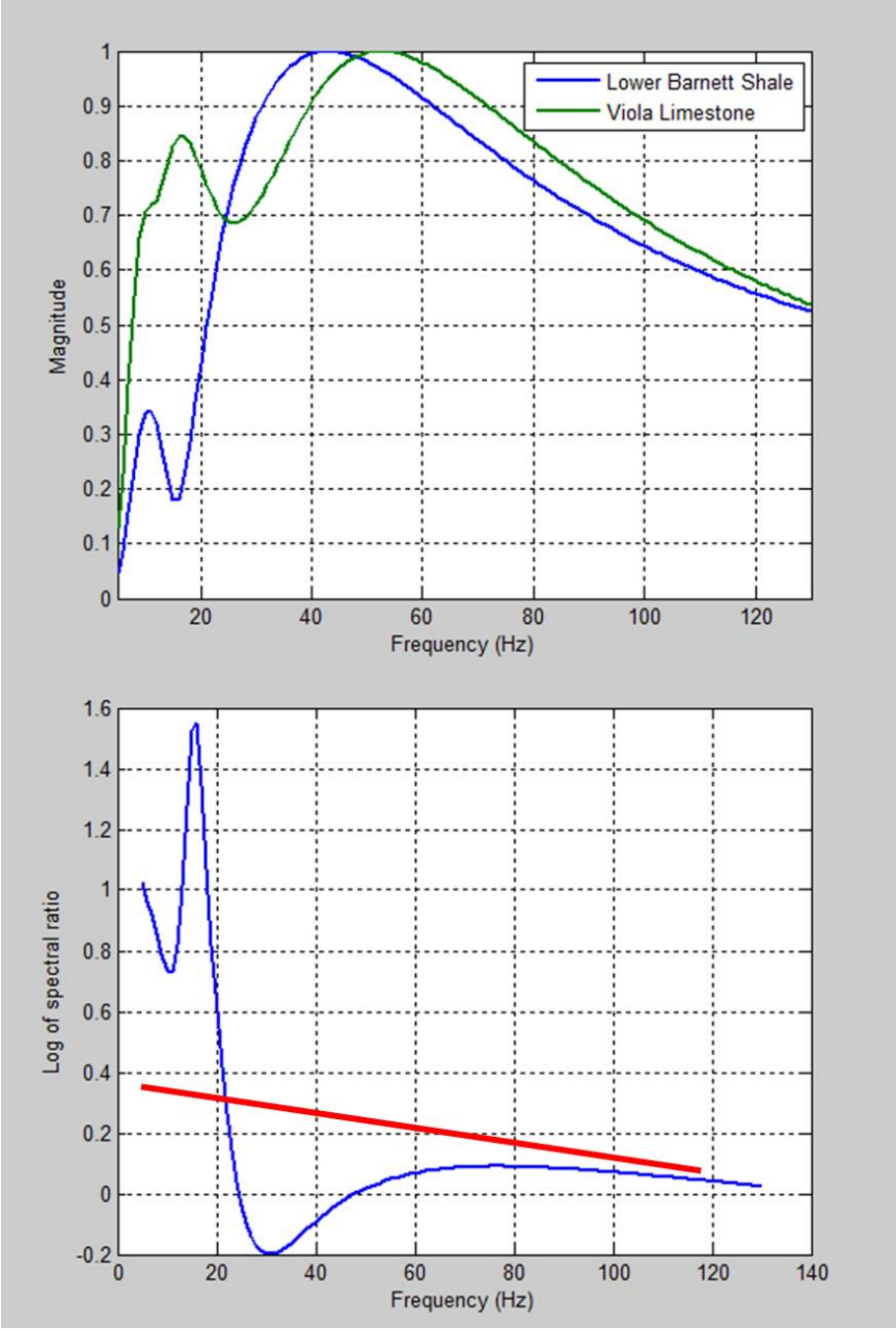

Figure 4.13. (a) Normalized spectra at two points on the top of the Lower Barnett Shale and Viola Limestone and (b) log of their spectral ratio. The red line indicates the trend of the curve.

the velocities. If the top of the Lower Barnett is improperly imaged due to an inaccurate velocity and if the Viola were accurately imaged, I would expect a broad band signal at the Viola, giving rise to a negative value of Q.

The travel times at different offsets sample different geology, thereby smearing any Q effect. My data are at a depth of about 7000 ft with a maximum offset of 14000 ft. For the Lower Barnett, vertically traveling energy travels 300 ft while the far offset energy incident at 45° travels 420 ft, thereby suffering greater attenuation. Q is laterally smeared over an area of 600 ft.

Rao and Wang (2009) find that attenuation is also closely associated with fractures. Fractures smaller than or equal to a half-wavelength of seismic acts as single diffraction points and in practice, with a limited frequency band, a significant number of small fractures may be missed and the attenuation measurement may be inaccurate. Tuning effects also give rise to spectral changes. Figures 4.16 shows a synthetic tuning model and its ICWT deconvolution which is close to the original model. Convolution of two opposite-sign reflection coefficients that are close to each other with the source wavelet is equivalent to a differentiator in time domain or amplifying the high frequencies.

Equal-sign reflection coefficients with the source wavelet is an integration operator in the frequency domain which preserves the low frequencies but attenuates higher frequencies. The shift from lower (Lower Barnett) to higher peak frequency (Viola) as shown in Figure 4.13 is frequently observed in the data and probably the result of thin beds. Such a shift produces an unrealistic negative Q value.

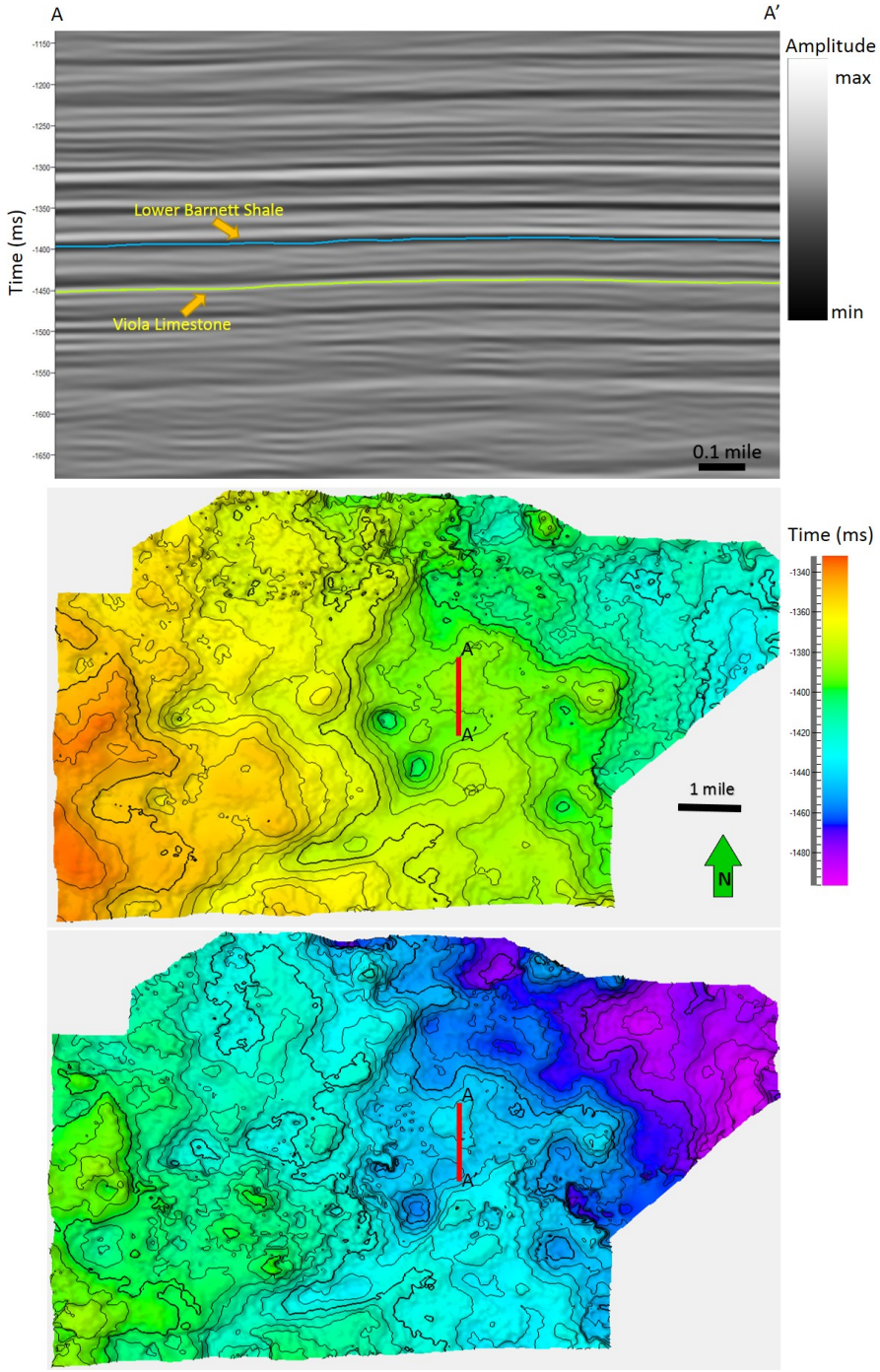

Figure 4.14. (a) Vertical slice of the seismic amplitude data, time structure map of the top of (b) the Lower Barnett Shale and (c) the Viola Limestone.

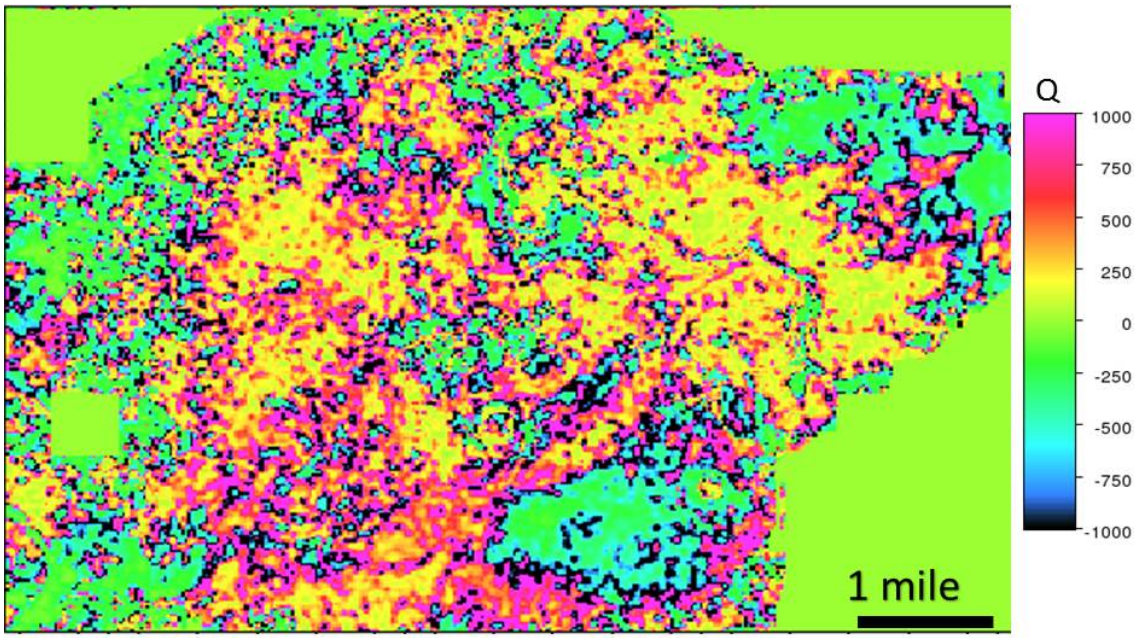

Figure 4.15. Quality factor Q computed between the top of the Lower Barnett Shale and top of the Viola limestone using equation 4.10 .

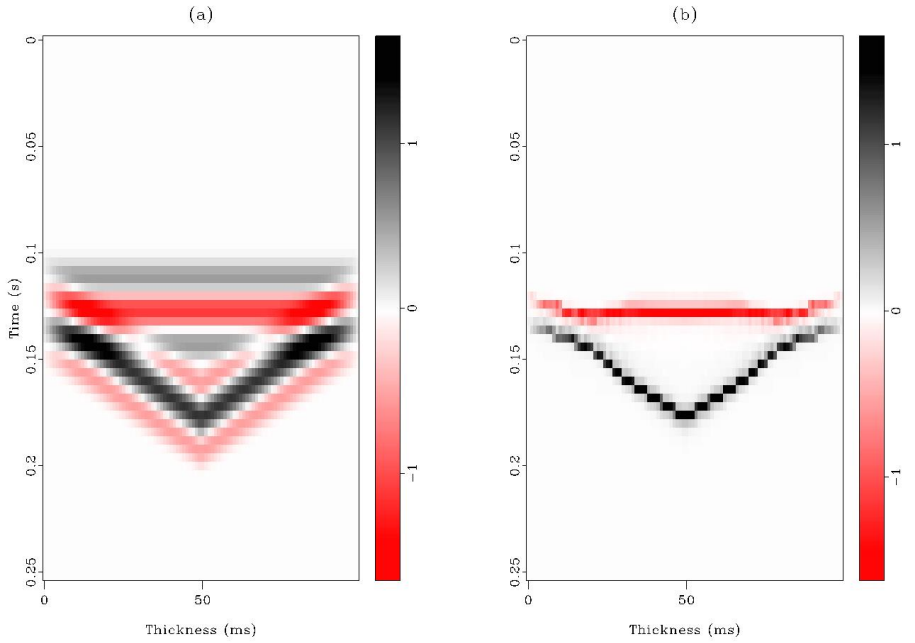

Figure 4.16. (a) Synthetic tuning model and (b) its corresponding ICWT deconvolution (after Matos and Marfurt, 2011).

Chapter 5

CONCLUSIONS

The ridges or connected singularities obtained from the Continuous Wavelet Transform contain the most important information in the data. The maxima wavelet matrix derived from the ridges makes up the basis to model the data in such a manner that the amplitude is preserved and the smaller events are updated into the model at later iteration. The first iteration of the maxima wavelet matching is equivalent to the Inverse Continuous Wavelet Transform deconvolution proposed by Matos and Marfurt (2011).

Spectral decomposition using the Continuous Wavelet Transform is able to detect the local change in amplitude and phase in greater detail and can therefore can be used to estimate attenuation. In principle, accurate spectral components should provide a means to estimate Q. I applied such a workflow to a Barnett Shale survey that was acquired after 400 wells were drilled and completed using hydraulic fracturing. My resulting Q images are difficult to interpret and perhaps inaccurate due to inaccurate velocities at the top and bottom of the reservoir. If the data are of good quality, the anomalous spectral behavior may be due to as yet poorly understood mechanics of gas charged, fractured shale. A number of factors were addressed as to why the methods did not work including data quality due to picking velocity, migration artifacts and the effects on frequencies of fractures and tuning effects. In addition, wide angle stack smears out the Q effect as the seismic wave at different offsets. A careful processing workflow is necessary in order to not alter the frequency response of the data and accurately estimate Q, such as high resolution velocity picking,

near-angle stack and non-stretch NMO.

REFERENCES

Aki, K., and P.G. Richards, 1980, Quantitative Seismology: Theory and Methods: W. H. Freeman & Co.

Azimi, S. A., A. V. Kalinin, V. V. Kalinin, and B. L. Pivovarov, 1968, Impulse and transient characteristics of media with linear and quadratic absorption laws: Izvestiya, Physics of the Solid Earth, **2**, 88-93.

Cole, K. S., and R. H. Cole, 1941, Dispersion and absorption in dielectrics: I. Alternating current characteristics: Journal of Chemical Physics, **9**, 342-351.

Costag, G. M., and K. R. Ernest, 1987, Seismic attenuation and Poisson's ratios in oil sands from crosshole measurements: Journal of the Canadian Society of Exploration Geophysicists, **23**, 46-55.

Futterman, W. I., 1962, Dispersive body waves: Journal of Geophysical Research, **67**, 5279-5291.

Guo, H., K. J. Marfurt, and J. Liu (2009), Principal component spectral analysis, Geophysics, **74**, 35-43.

Hauge, P., 1981, Measurements of attenuation from vertical seismic profles: Geophysics, **46**, 1548-1558.

Johnston, D. H., and M. N. Toksöz, 1974, Definitions and terminology in Seismic Wave Attenuation: Geophysics Reprint Series, **2**, Society of Exploration Geophysics.

Kjartansson, E., 1979, Constant Q-wave propagation and attenuation: Journal of Geophysical Research, **84**, 4737-4748.

Kolsky, H., 1955, The propagation of stress pulses in viscoelastic solid: Philosophical Magazine, **1**, 691-710.

Liner, C. C., 2012, Elements of Seismic Dispersion: A Somewhat Practical Guide to Frequency-dependent Phenomena: Society of Exploration Geophysicists.

Liu, J. L., and K. J. Marfurt, 2007, Instantaneous spectral attributes to detect channels: Geophysics, **72**, 23-31.

Mallat, S., 2009, A wavelet tour of signal processing: Academic Press.

Matos, M. C., and K. J. Marfurt, 2011, Inverse continuous wavelet transform deconvolution: 81st Annual International Meeting of the SEG, Expanded Abtracts, 1861-1865

Morlet, J., G. Arens, E. Fourgeau and D. Giard, 1982, Wave propagation and sampling theory - Part II: Sampling theory and complex waves, Geophysics, **47**, 222-236.

M*ü*ller, G., 1983, Rheological proporties and velocity dispersion of a medium with power-law dependence of **Q** on frequency: Journal of Geophysical Research, **54**, 2029.

Rao, Y. and Y. Wang, Fracture effects in seismic attenuation images reconstructed by waveform tomography: Geophysics, **74**, 2534.

Reine, C., M. van der Baan, and C. Roger (2009), The robustness of seismic attenuation measurements using fixed- and variable-window time-frequency transforms: Geophysics, **74**, 123-135.

Strick, E., 1967, The determination of Q, dynamic viscosity and transient creep curves from wave propagation measurements: Geophysical Journal. Royal Astronomical Society, **13**, 197-218.

Tonn, R., 1991, The determination of the seismic quality factor Q from VSP data: A comparison of different computational methods: Geophysical Prospecting, **39**, 1-27

Ursin, B., and T. Toverud, 2002, Comparison of seismic dispersion and attenuation models: Studia Geophysica et Geodaetic, **46**, 293-320.

Van der Baan M., 2012 Bandwidth enhancement: Inverse Q filtering or time-varying Wiener deconvolution?: Geophysics, **77**, 133-142.

Wang, Y., and J. Guo, 2004, Modified Kolsky model for seismic attenuation and dispersion: Journal of Geophysics and Engineering, **1**, 187-196.

Wang, Y., 2008, Seismic inverse Q Filtering: Blackwell Publishing.

Appendix A

THE CONTINUOUS WAVELET TRANSFORM

A.1 Definitions

The Continuous Wavelet Transform (CWT) is a time-frequency method that decomposes a signal into duration-limited, band-passed components (Mallat, 2009). Higher-frequency components are short-duration, broad-band while low frequency components are long-duration, narrow-band signals. The CWT is an excellent tool to analyze non-stationary seismic signal, providing useful information of time-frequency localization. An advantage of the CWT is that one can design a mother wavelet $\Psi(t)$ depending on the nature of the signal and the features one wishes to detect, provided that the wavelet satisfies the following conditions:

1. Absolute integrability,

$$\int |\Psi(t)|dt < \infty, \tag{A.1}$$

2. Square integrability or finite energy,

$$\int |\Psi(t)|^2 dt < \infty, \text{ and} \tag{A.2}$$

3. Admissibilty or zero DC-component,

$$\int \Psi(t)dt = 0. \tag{A.3}$$

The wavelet at scale a and centered at time τ is given by

$$\psi_{a,\tau}(t) = \frac{1}{\sqrt{a}}\Psi(\frac{t-\tau}{a}). \tag{A.4}$$

The CWT of a signal $d(t)$ is defined by:

$$c(a,\tau) =< s, \Psi_{a,\tau} >\equiv \frac{1}{\sqrt{a}}\int s(t)\psi^*(\frac{t-\tau}{a})dt, \tag{A.5}$$

where ψ^* denotes the complex conjugate of ψ.

The inverse transform is performed by integrating over all scales and delay times:

$$d(t) = \frac{1}{C_\Psi}\int c(a,b)\frac{1}{\sqrt{a}}\Psi(\frac{t-\tau}{a})\frac{da}{a^2}d\tau, \tag{A.6}$$

where C_Ψ is a constant associated with the wavelet and is defined by

$$C_\Psi = \int_0^{+\infty}\frac{|\hat{\Psi}(\omega)|^2}{\omega}d\omega, \tag{A.7}$$

where $\hat{\Psi}(\omega)$ denotes the Fourier transform of $\Psi(t)$.

For a real signal $d(t)$, the inverse transform can be computed as

$$d(t) = \frac{2}{C_\Psi}\mathrm{Re}\Big[\int c(a,\tau)\frac{1}{\sqrt{a}}\psi(a,\tau)\frac{da}{a^2}d\tau\Big]. \tag{A.8}$$

A.2 The CWT applied to spectral analysis

Equations A.5 and A.8 are useful in data compression and filtering, and are commonly used in suppressing air wave noise. As interpreters, we are also interested in time-frequency analysis that quantifies the localization of frequencies in time. To do so, given a mother wavelet with centered frequency 1Hz, I

replace the scale a with $\frac{1}{f}$ where f is the central frequency of the wavelet. Then the CWT will have the form

$$c(f,\tau) = \sqrt{f}\int d(t)\Psi^*(f(t-\tau))dt, \tag{A.9}$$

while its corresponding inverse transform has the form

$$d(t) = \frac{1}{C_\Psi}\int c(f,\tau)\sqrt{f}\Psi(f(t-\tau))df d\tau. \tag{A.10}$$

A.3 The Morlet wavelet

This thesis and much CWT work use Morlet wavelets. A complex Morlet wavelet in the time domain is given by

$$\Psi_{\beta,f_c}(t) = \frac{\beta}{\sqrt{\pi}}\Big[\exp\Big(2\pi i f_c t\Big)\exp\Big(\frac{-\beta^2 t^2}{2}\Big) - \exp\Big(-2\beta^2\Big)\Big], \tag{A.11}$$

where $\frac{1}{\beta}$ is the standard deviation or the time-bandwidth and f_c is the central frequency of the wavelet in Hz. In practice, $\exp\Big(-2\beta^2\Big)$ is very small for the value of β I use that the wavelet becomes approximately but not strictly admissible.

Figure A.1 shows a Morlet wavelet whose frequency bandwidth, $\beta = 1.15$ Hz and the central frequency, $f_c = 3.0$ Hz.

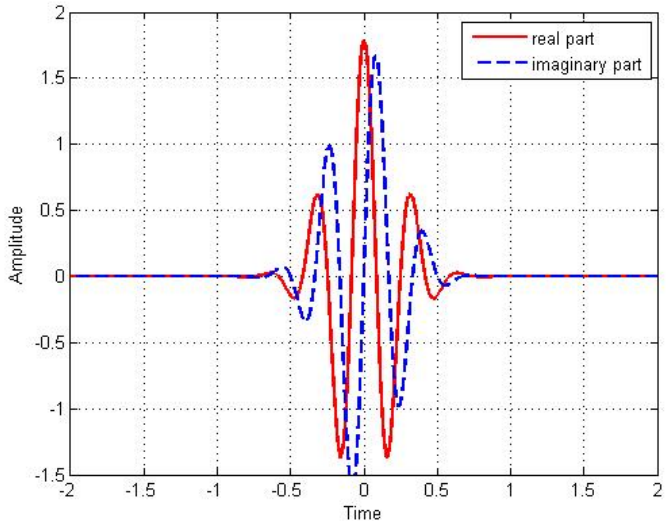

Figure A.1. A Morlet wavelet with $\beta = 1.15$, $f_c = 3.0$ Hz.

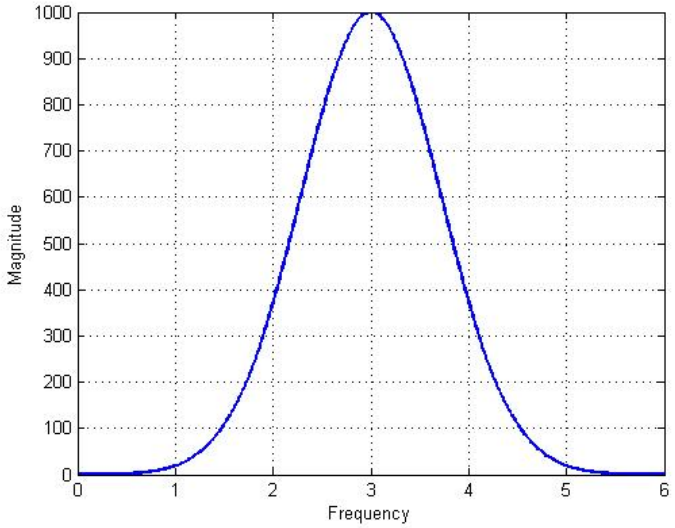

Figure A.2. The spectrum of the Morlet wavelet in Figure A.1.

Appendix B

PRINCIPAL COMPONENT ANALYSIS

Principal Component Analysis (PCA) is a linear orthogonal transformation, $\mathbf{P} = \begin{bmatrix} \mathbf{p}_1 & \mathbf{p}_2 & \cdots \mathbf{p}_m \end{bmatrix}^T$, that transforms a set of correlated observations, $\mathbf{X} = \begin{bmatrix} \mathbf{x}_1 & \mathbf{x}_2 & \cdots \mathbf{x}_n \end{bmatrix}$ where the vector $\mathbf{x}_j$ is the j^{th} observation, to a new domain such that the transformed data, $\mathbf{Y} = \begin{bmatrix} \mathbf{y}_1 & \mathbf{y}_2 & \cdots \mathbf{y}_n \end{bmatrix}$, consist of only uncorrelated events. The relationship between $\mathbf{X}$ and $\mathbf{Y}$ is represented by:

$$\mathbf{PX} = \mathbf{Y}. \tag{B.1}$$

The set of all vectors $\mathbf{p}_j$ makes up the principal components of $\mathbf{X}$. Each vector $\mathbf{y}_j$ is the projection $\mathbf{x}_j$ onto all the principal components $\mathbf{p}_k$.

To calculate $\mathbf{P}$, we first compute the covariance matrix of $\mathbf{X}$, $\mathbf{C_X}$:

$$\mathbf{C_X} = \frac{1}{n}\mathbf{X}\mathbf{X}^T, \tag{B.2}$$

where the element $C_X(i, j)$ is the cross-correlation between two observation $\mathbf{x}_i$ and $\mathbf{x}_j$.

The covariance matrix in the transformed domain, $\mathbf{C_Y}$, is related to $\mathbf{C_X}$ by:

$$\mathbf{C_Y} = \mathbf{P}\mathbf{C_X}\mathbf{P}^T \tag{B.3}$$

where $\mathbf{C_Y}$ is a diagonal matrix since $\mathbf{Y}$ consists of uncorrelated events.

$\mathbf{C_X}$ is a symmetric positive definite matrix. Therefore, its eigenvector matrix

$\mathbf{V}$ is an orthonormal matrix and satisfies $\mathbf{V}^T = \mathbf{V}^{-1}$. It can be verified that $\mathbf{P} = \mathbf{V}$ is a solution to equation B.3.

By picking $\mathbf{P} = \mathbf{V}$, $\mathbf{P}$ can be rewritten as the sum of weighted outer-products of the principal components (eigenvalue decomposition):

$$\mathbf{P} = \sum_{j=1}^{m} e_j \mathbf{p}_j \mathbf{p}_j^T, \tag{B.4}$$

where $\mathbf{e}_j$ is the eigenvalue associated with the eigenvector $\mathbf{p}_j$.

Substituting equation B.4 into equation B.1 gives:

$$\mathbf{Y} = \left[\sum_{j=1}^{m} e_j \mathbf{p}_j \mathbf{p}_j^T \right] \mathbf{X}. \tag{B.5}$$

Without loss of generality, suppose the eigenvalues e_j's are sorted in descending order $e_1 > e_2 > \cdots > e_m > 0$. Then define $\mathbf{Y}_k$ to be the partial sum of $\mathbf{Y}$:

$$\mathbf{Y}_k = \left[\sum_{j=1}^{k} e_j \mathbf{p}_j \mathbf{p}_j^T \right] \mathbf{X}. \tag{B.6}$$

In practice, assuming that the large variance is associated with important structures and small variance is associated with noise, limiting the number of terms in the sum is a filter that enhances the SNR.

PCA can be extended to apply to complex data. The mathematics is the same as for real data, except the covariance matrix of $\mathbf{X}$, $\mathbf{C}_\mathbf{X}$, is a self-adjoint matrix: $\mathbf{C}_\mathbf{X} = \mathbf{C}_\mathbf{X}^H$.

Appendix C

GRAPHICAL USER INTERFACES (GUIs)

While the main body of the thesis defines the theory, workflow and application of Q estimation, the major work is behind the scenes. Specifically I have written FORTRAN 90 application programs spectral decomposition using the continuous wavelet transform **spec_cwt** and **estimate_q**. I have also significantly modified application programs **complex_stratal_slice** and **complex_pca_spectra** to interpolate and precondition the complex spectra stratal slices that serve as input to Q estimation.

Each application requires a shell script and a graphical user interface. Source code has been distributed to our sponsors and resides on our OU AASPI hardware. In this Appendix I will provide a discussion of the GUIs for those who wish to use my technology. Figure C.1 illustrates the general workflow of the entire programs.

C.1 The aaspi_spec_cwt GUI

- (1) Browse to the input file location
- (2) Assign a unique project name, typically common to all attributes generated from a given seismic data volume
- (3) Add an suffix that defines a given set of parameters or filtered version of the input data
- (4) Choose the lowest frequency $f1$, highest frequency $f4$ and frequency step df thereby defining the CWT spectral components

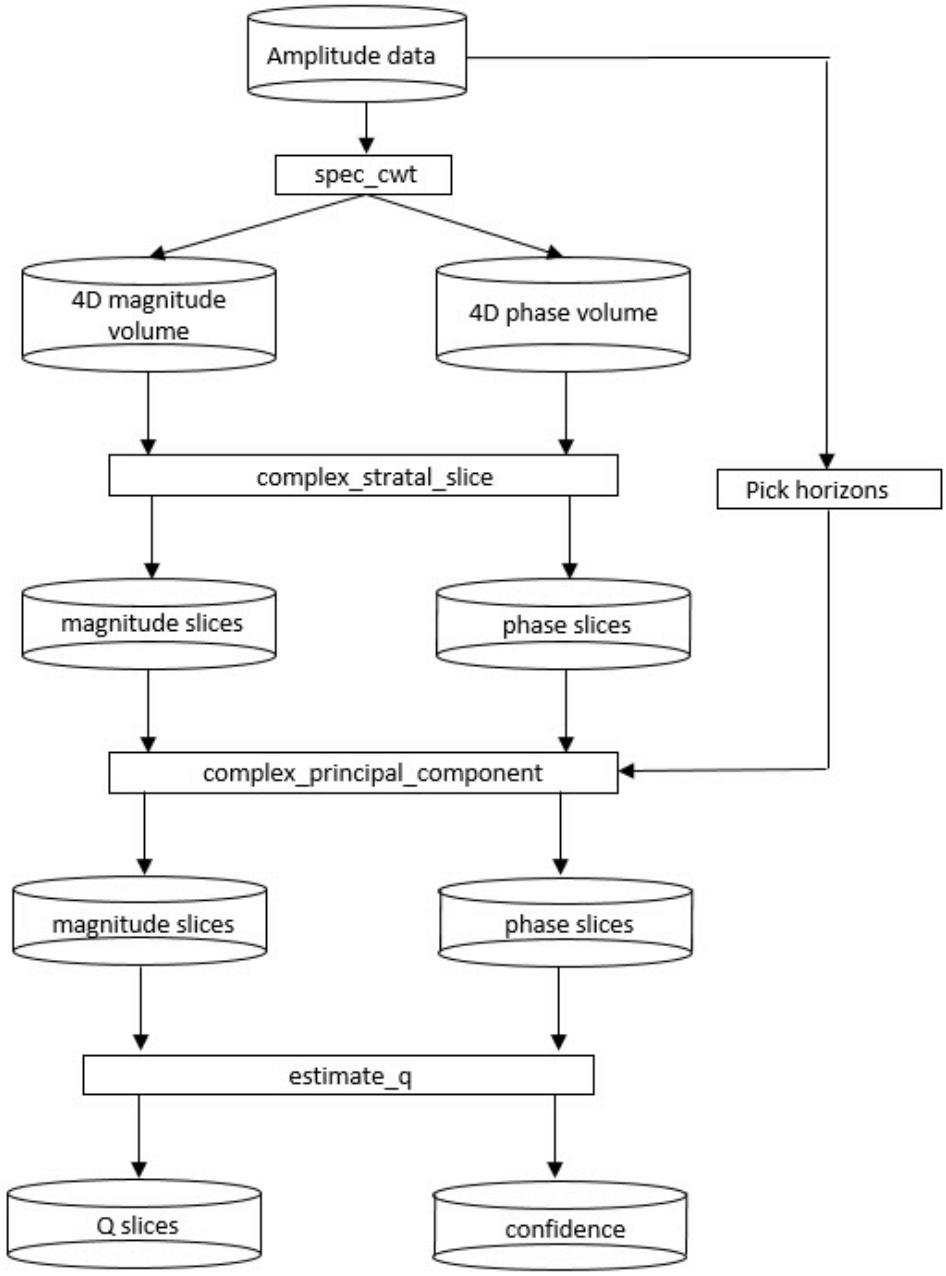

Figure C.1. Q estimation flow chart.

- (5) Check the box if you want the output spectral magnitude and/or phase as a 4D cube in the order t, f, cdp_no, line_no
- (6) Check the box if you want the output magnitude components
- (7) Check the box if you want the output phase components
- (8) Click to change the tab to modify MPI and other less commonly modified variables
- (9) Check the box if you wish to use MPI
- (10) Enter the number of processors per node
- (11) Enter the list of nodes, separated by blanks. Default=localhost
- (12) Check the box if you want verbose output for debugging
- (13) Enter the range for output inline and crossline ranges.

C.2 The aaspi_complex_stratal_slice GUI

- (1) Browse to the 4D spectral magnitude and spectral phase volume previously generated by program spec_cwt or spec_cmp
- (2) Browse to input the upper and lower stratal surfaces saved in Earth Vision format.
- (3) Define the number of output slices, minimum is 2
- (4) Enter an unique project name and suffix
- (5) Enter times to either include or exclude the waveform along the picked horizons. A positive value will be added to the horizon.

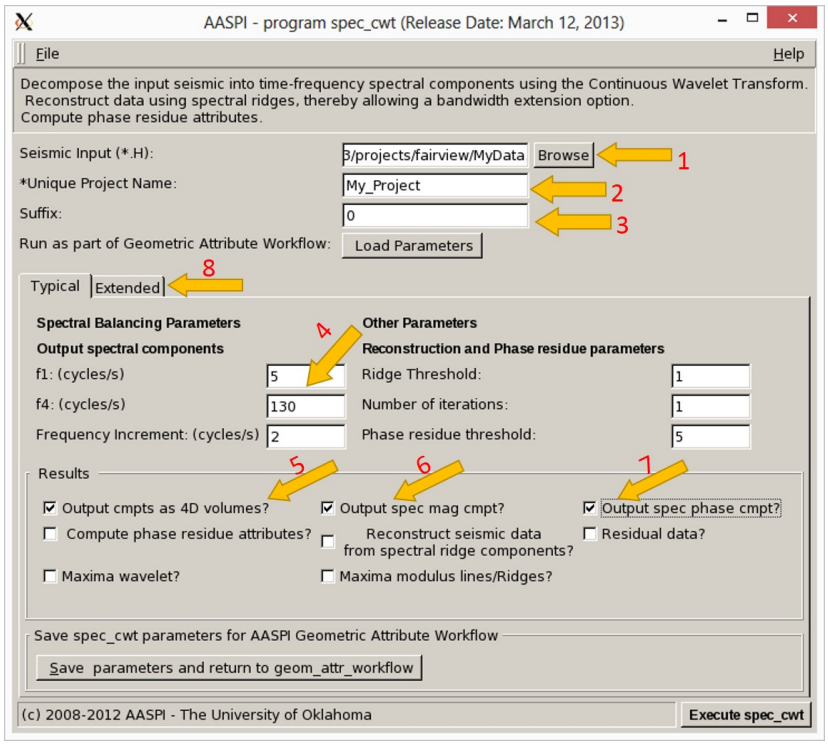

Figure C.2. The **aaspi_spec_cwt** GUI.

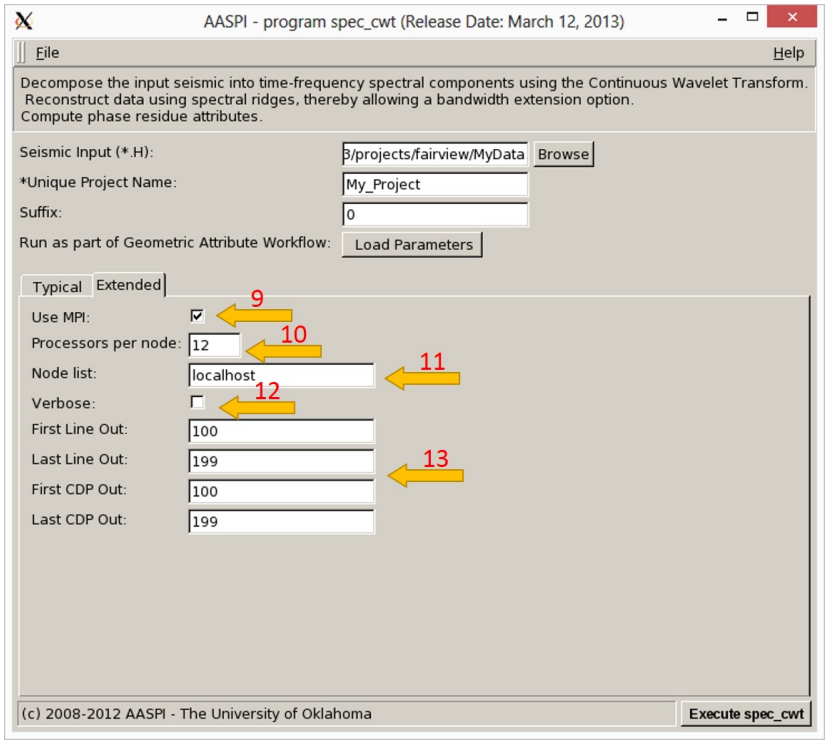

Figure C.3. The **aaspi_spec_cwt** GUI.

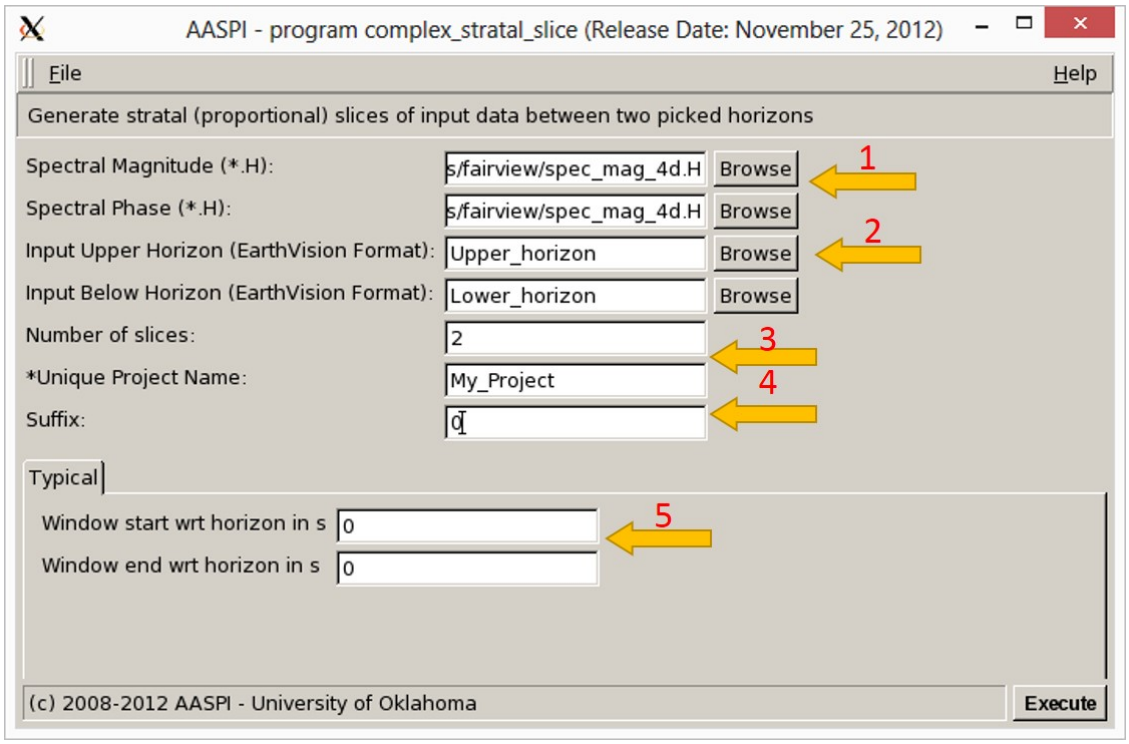

Figure C.4. The **aaspi_complex_stratal_slice** GUI.

C.3 The aaspi_complex_pca_spectra GUI

- (1) Browse and find the spectral magnitude and spectral phase stratal slice input files
- (2) Enter a unique project name and suffix
- (3) Start time and end time will be read automatically from the input files
- (4) Enter the lowest and highest frequency (in Hz) to be analyzed
- (5) Enter number of principle components to generate
- (6) Check the boxes for output file options.

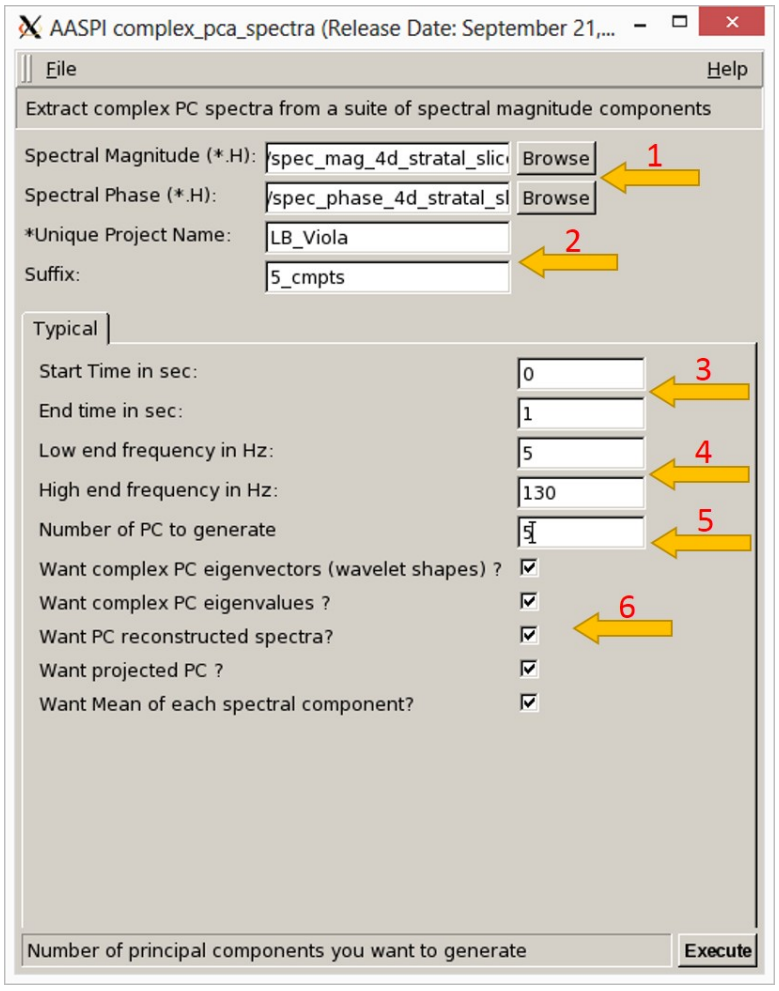

Figure C.5. The **aaspi_complex_pca_spectra** GUI.